

A concurrent atomistic-crystal plasticity multiscale model for crack propagation in crystalline metallic materials

Subhendu Chakraborty^{a,1}, Somnath Ghosh^{b,2,*}

^a Department of Mechanical Engineering, Johns Hopkins University, United States of America

^b Departments of Civil & Systems, Mechanical, and Materials Science & Engineering, Johns Hopkins University, 3400 N. Charles Street, Baltimore, MD 21218, United States of America

Received 17 July 2020; received in revised form 20 February 2021; accepted 20 February 2021

Available online 12 March 2021

Abstract

This paper develops a coupled concurrent atomistic–continuum multiscale model for analyzing crack propagation and associated mechanisms in crystalline metallic materials. This modeling framework can be used to develop effective continuum-scale constitutive models for crack evolution in deforming domains characterized by crystal plasticity. The atomistic region is modeled by the molecular dynamics (MD) code LAMMPS, while the continuum region is modeled by a dislocation density crystal plasticity FE model. A novel method is developed to transfer discrete dislocations in the atomistic domains to dislocation densities in the continuum domain. Propagation of dislocation densities in the continuum domain is modeled by the advection equation of a conserved quantity using the reproducing kernel particle method (RKPM) in conjunction with the collocation method. Validation studies are conducted by comparing results of the concurrent model with those by MD for nickel single crystal specimen with an embedded crack. An analytical model of the crack tip nucleated dislocation density evolution is developed for inclusion in crystal plasticity models. The effect of applied strain-rate and temperature on the parameters of this model are studied.

© 2021 Elsevier B.V. All rights reserved.

Keywords: Concurrent atomistic-crystal plasticity model; Crack propagation; Dislocation densities; Advection equation; Reproducing kernel particle method; Single crystal Nickel

1. Introduction

Modeling plastic deformation and crack growth in polycrystalline material microstructures is important for understanding ductile fracture of metallic materials. This phenomenon involves complex mechanisms of crack nucleation, growth and deformation mechanisms, including inter-atomic decohesion, dislocation nucleation, mobility and interactions. They traverse a range of spatial scales, from the atomic scale of crack nucleation and propagation to the continuum scales of short crack propagation and plastic deformation in the crystalline microstructure. A shortcoming with many of the conventional models, coupling crack growth with crystal plasticity, is the lack

* Corresponding author.

E-mail address: sghosh20@jhu.edu (S. Ghosh).

¹ Graduate Research Associate.

² M. G. Callas Professor.

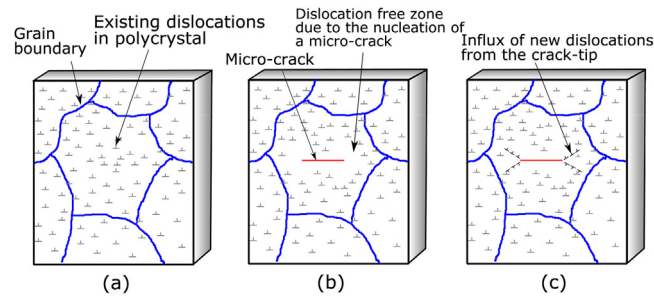


Fig. 1. Schematic representation of the interaction between a crack and dislocations inside a grain: (a) polycrystalline domain containing preexisting dislocations, (b) micro-crack nucleated inside a grain creating a localized dislocation-free zone near the crack, (c) crack acting as a potential source of new dislocation nucleation.

of consistency with underlying physics. Conventional cohesive zone models [1–3] for example, lack consistent coupling of mechanisms in the process zone. Dislocations nucleate from crack tips and contribute to the deformation mechanisms near the crack zone. At the atomic scale, crack growth is related to the irreversibility of plastic deformation and other crack tip mechanisms. Fig. 1 is a schematic representation of the typical interplay between a crack and dislocations. A polycrystalline metallic material consists of pre-existing dislocations inside grains as shown in Fig. 1(a). Under monotonic or cyclic mechanical loading, material deformation takes place by elastic bond stretching and plastic slip due to the pre-existing dislocations. Dislocation density evolves mainly due to the expansion of the dislocation loop and subsequent interaction with other dislocations. As dislocations start to form a cluster around a localized region within a grain, the region becomes a potential location for nucleating a micro-crack as depicted in Fig. 1(b). The high stress gradients around the crack tip create a dislocation-free local region, which in turn are either driven further due to the high shear stresses near the crack tip or are annihilated at the crack surface. With further loading, the crack-tip becomes a potential source of new dislocations as shown in Fig. 1(c). The nucleated dislocations play a major role in the material deformation and failure response. These mechanisms are typically not accounted for, in conventional crystal plasticity and crack growth models. A concurrent multiscale framework, coupling atomistic models of crack evolution with continuum scale deformation can overcome some of the shortcomings faced in failure modeling of crystalline solids.

Pure atomistic simulations using molecular statics (MS) or molecular dynamics (MD) have been used to investigate crack induced plastic deformation mechanisms in crystalline metallic materials, e.g. in [4–7]. Despite advances in high-performance computing, large-scale MD simulation of crack propagation in larger domains that correspond to continuum length and time scales remains a significant challenge. Concurrent analysis, coupling continuum and atomistic models can partially circumvent this limitation. Critical regions of extreme events are modeled at the atomic scale using MS or MD, while the parts of the domain are modeled using continuum-scale constitutive relations. An overview of the various methods in the literature that couple atomic and continuum scale models is given in [8]. The methods use different continuum scale models, as well as information passing methods between the discrete and continuum domains. The continuum region has been modeled using linear elasticity in [9–12] and nonlinear elasticity in [13–15]. Dislocation-based plasticity has been incorporated in the models of [16–18]. In [16] a coarse-graining technique using rhombohedral 3D element is introduced with the element boundary coinciding with slip planes of a fcc crystal to facilitate the passage of dislocations from the atomic to the continuum domains. In [17] the nonlocal quasi-continuum method in [19] is extended to incorporate an adaptive refinement of a local continuum region up to the atomic resolution to enable defect migration. A coupled atomistic/discrete dislocation or CADD-3D method has been developed in [18], where 3D discrete dislocation dynamics is used to model plasticity in the continuum region. An atomistic template of the dislocation core structure is used to transfer dislocations from the atomistic to the continuum region at the interface. Each dislocation topology is explicitly represented in 3D and tracked individually in the continuum domain. This can however increase the computational cost significantly as the simulation progresses, due to the continuous dislocation influx from the atomistic to the continuum region. Alternatively, transforming the discrete dislocation influx to effective continuum dislocation densities for incorporation in constitutive relations e.g. in [20,21] can significantly mitigate the computational overhead.

This paper develops a concurrent atomistic-crystal plasticity model for crack propagation in crystalline metallic materials. The concurrent modeling framework builds upon previous models of elasticity in [13–15]. The continuum domain is modeled by a dislocation density crystal plasticity model given in [21–24], while the atomistic domain is modeled by molecular dynamics (MD) using an embedded atom model (EAM)-based potential [6]. An important feature of this concurrent model for plasticity is the simultaneous transfer, transformation and transport of dislocations across the atomic–continuum interface. This process involves:

- Identify, characterize and quantify discrete dislocations from atomic configurations in atomistic simulations following the DXA method developed in [25] and implemented in [6];
- Subsequently, transfer atomic-domain discrete dislocations at the interface to transformed dislocation densities in the continuum domain;
- Once manifested, propagate dislocation densities in the continuum domains.

Dislocation transport in the continuum domain is conducted by solving the advection equation. Large spatial gradients in dislocation densities accompany dislocation cores, necessitating highly refined mesh for conventional FE solution of the advection equation. This makes the FE solution of dislocation propagation computationally prohibitive. To avert this, the reproducing kernel particle method (RKPM) [26,27], along with point collocation and nodal integration technique is used to solve the advection equation. The concurrent model is used to study crack evolution in single crystal Nickel (Ni) along with dislocation nucleation from the crack tip and its manifestation as dislocation density.

The paper is arranged as follows. Section 2 establishes the framework of the concurrent atomistic–continuum model. Section 3 discusses the dislocation density crystal plasticity model for the continuum domain, while the time-accelerated molecular dynamics (MD) model for the atomistic domain is outlined in Section 4. Transformation and domain transfer of nucleated dislocations at the interface is discussed in Section 5, and propagation of nucleated dislocation density in the continuum domain is detailed in 6. Section 7 develops the concurrent atomistic-crystal plasticity model with validation in Section 8. In Section 9, the concurrent model is used to study the evolution of the nucleated dislocation density and develop an analytical evolution law. The paper concludes with a summary in Section 10.

2. Framework of the concurrent atomistic–continuum model

A concurrent atomistic–continuum model, coupling a molecular dynamics (MD) model with a crystal plasticity finite element model (CPFEM) under quasi-static loading conditions, is developed in this study. The coupled modeling framework, depicted in Fig. 2, is based on a structure initially proposed in [13,14]. Three computational sub-domains are integral to the concurrent model, viz. (i) the atomistic domain of MD simulations Ω_A , (ii) the continuum domain of crystal plasticity finite element (FE) simulations Ω_C , and (iii) an overlapping interface domain $\Omega_I (= \Omega_A \cap \Omega_C)$. The MD simulations are carried out by the parallel Large-scale Atomic/Molecular Massively Parallel Simulator *LAMMPS* [28]. Constitutive parameters of the finite deformation crystal plasticity FE model in Ω_C are calibrated from self-consistency conditions with the MD results. Inertia effects are neglected for the quasi-static FE analysis. The interface domain Ω_I is comprised of overlapping layers of the FE and MD domains. It provides a zone for imposing traction reciprocity and kinematic compatibility constraints between the MD and FE simulation domains. Each FE node β in Ω_I is associated with a group of contiguous underlying atoms, located inside of a 3D Voronoi cell neighborhood G_β of that node. The Voronoi cells are generated by tessellations involving neighboring nodes in Ω_I , following steps discussed in [29]. Compatibility conditions are enforced between each interface FE node β and the associated group of interface atoms in $G_\beta \in \Omega_I$. For atom-node compatibility, the displacements of an interface FE node are equated to the spatially-averaged displacements of the associated interface atoms. The following subsections discuss the FE and MD formulations, as well as the interface constraints.

2.1. Updated Lagrangian FE model for finite deformation crystal plasticity in the continuum domain

A summary of the finite deformation elasto-plasticity finite element model is given in this section. Specific inputs for the crystal plasticity constitutive model are drawn from Section 3 and Appendix. An updated Lagrangian (UL) formulation [30] is invoked for solving this problem under quasi-static conditions, where the solution is obtained

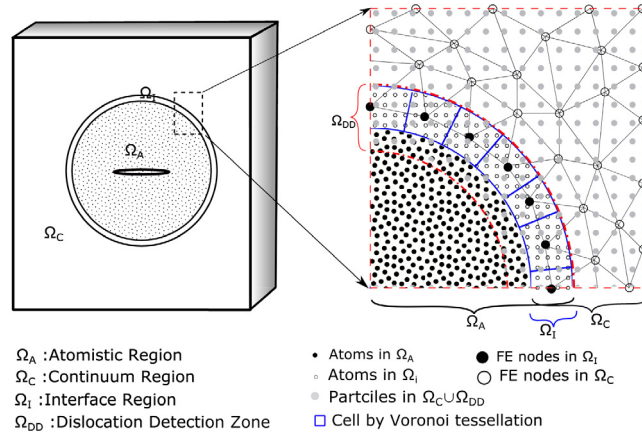


Fig. 2. Schematic representation of the computational domain for concurrent atomistic–continuum simulations, showing models for the atomistic, continuum and interface regions.

incrementally at discrete points in the time domain. In the UL formulation, the principle of virtual work for an increment transcending discrete temporal points t and $t + \Delta t$ is written as:

$$\int_{\Omega_C^t} \delta \mathbf{E}_t^{t+\Delta t} : \mathbf{S}_t^{t+\Delta t} d\Omega_C^t = W R_{ext}^{t+\Delta t} \quad (1)$$

where Ω_C^t is the continuum domain at time t , which corresponds to the reference configuration for the UL formulation. The variables $\mathbf{E}_t^{t+\Delta t}$ and $\mathbf{S}_t^{t+\Delta t}$ respectively are the Green–Lagrange strain and the second Piola–Kirchhoff (PK) stress tensors at time $t + \Delta t$, with respect to the reference configuration at time t and $W R_{ext}^{t+\Delta t}$ is the external virtual work at time $t + \Delta t$. δ corresponds to the first variation of the associated variable. The updated variables at time $t + \Delta t$ are given in terms of their values at time t and the incremental values (with prefix Δ) to be solved, as follows.

$$\text{Displacement : } \mathbf{u}^{t+\Delta t} = \mathbf{u}^t + \Delta \mathbf{u} \quad (2a)$$

$$\text{Green–Lagrange Strain : } \mathbf{E}_t^{t+\Delta t} = \Delta \mathbf{E}^t = \Delta \mathbf{e}^t + \Delta \boldsymbol{\eta}^t, \quad (2b)$$

$$\text{where } \Delta \mathbf{e}^t = \frac{1}{2} \left[\left(\frac{\partial \Delta \mathbf{u}}{\partial \mathbf{x}^t} \right)^T + \frac{\partial \Delta \mathbf{u}}{\partial \mathbf{x}^t} \right] \text{ and } \Delta \boldsymbol{\eta}^t(\Delta \mathbf{u}) = \frac{1}{2} \left(\frac{\partial \Delta \mathbf{u}}{\partial \mathbf{x}^t} \right)^T \frac{\partial \Delta \mathbf{u}}{\partial \mathbf{x}^t} \quad (2c)$$

$$\text{2nd Piola–Kirchhoff Stress : } \mathbf{S}_t^{t+\Delta t} = \mathbf{S}_t^t + \Delta \mathbf{S}^t = \boldsymbol{\sigma}^t + \Delta \mathbf{S}^t, \quad (2d)$$

$$\text{where } \mathbf{S}_t^{t+\Delta t} = J_t^{t+\Delta t} (\mathbf{F}_t^{t+\Delta t})^{-1} \boldsymbol{\sigma}^{t+\Delta t} (\mathbf{F}_t^{t+\Delta t})^{-T} \quad (2e)$$

$$\text{Stress–Strain Relation : } \Delta \mathbf{S}^t = \mathbb{C}^t(\mathbf{u}) : \Delta \mathbf{E}^t(\mathbf{u}) \quad (2f)$$

In these relations, the superscript t corresponds to the variable at the beginning of the increment, while superscript $t + \Delta t$ corresponds to the variable at the end of the increment. \mathbf{u} is the displacement, $\boldsymbol{\sigma}$ is the Cauchy stress tensor, $\mathbf{F}_t^{t+\Delta t}$ is the deformation gradient at time $t + \Delta t$ with respect to the reference configuration at time t , and $J_t^{t+\Delta t}$ is its determinant or Jacobian. \mathbb{C}^t is the local material tangent stiffness matrix at time t . For the crystal plasticity equations described in Section 3, the explicit form of the \mathbb{C}^t matrix is derived in [Appendix](#). The increment of the Green–Lagrange strain tensor is decomposed into a linear part $\Delta \mathbf{e}^t(\Delta \mathbf{u})$ and a nonlinear part $\Delta \boldsymbol{\eta}^t(\Delta \mathbf{u})$ in Eq. (2c). The external virtual work in Eq. (1) is expressed as:

$$W R_{ext}^{t+\Delta t} = \int_{\Omega_C^t} \delta \mathbf{u}^{t+\Delta t} \cdot \mathbf{b}^{t+\Delta t} d\Omega_C^t + \int_{\Gamma_\sigma^t} \delta \mathbf{u}^{t+\Delta t} \cdot \mathbf{t}^{t+\Delta t} d\Gamma_\sigma^t \quad (3)$$

where \mathbf{b} is the body force per unit volume. The continuum domain boundary $\partial \Omega_C^t$ is comprised of an external traction boundary Γ_σ^t on which the traction \mathbf{t} is the prescribed and a complementary boundary segment that interfaces with the atomistic domain that is constrained by atomic forces. Substituting the incremental forms of variables in Eq. (2)

into the principle of virtual work in Eq. (1) yields a scalar-valued function G , representing the incremental weak form as:

$$G^t(\Delta \mathbf{u}, \delta \mathbf{u}) = \int_{\Omega_C^t} \delta \mathbf{e}^t : \mathbb{C}^t : \Delta \mathbf{E}^t d\Omega_C^t + \int_{\Omega_C^t} \delta \boldsymbol{\eta}^t : \mathbb{C}^t : \Delta \mathbf{E}^t d\Omega_C^t + \int_{\Omega_C^t} \delta \mathbf{e}^t : \boldsymbol{\sigma}^t d\Omega_C^t + \int_{\Omega_C^t} \delta \boldsymbol{\eta}^t : \boldsymbol{\sigma}^t d\Omega_C^t - W R_{ext}^{t+\Delta t} = 0 \quad (4)$$

The modified Newton–Raphson iteration method [30] is invoked to solve the nonlinear equation (4) for the displacement increment $\Delta \mathbf{u}$, along with the associated variables. This process requires the linearization of the function $G(\Delta \mathbf{u}^i, \delta \mathbf{u})$ with respect to the displacement increment $\Delta \mathbf{u}$. For the i th iteration step in the solution method, the linearization is expressed as:

$$G^t(\Delta \mathbf{u}^i, \delta \mathbf{u}) + \mathbf{D}G^t(\Delta \mathbf{u}^i, \delta \mathbf{u}) \cdot d\mathbf{u} = 0 \quad (5)$$

where $d\mathbf{u} = \Delta \mathbf{u}^{i+1} - \Delta \mathbf{u}^i$ is the iterative corrector to the displacement increment and $\mathbf{D}G \cdot d\mathbf{u} (= \frac{\partial}{\partial \varepsilon} [G(\Delta \mathbf{u}^i + \varepsilon d\mathbf{u}, \delta \mathbf{u})]_{\varepsilon=0})$ corresponds to the directional derivative of G in the direction of the displacement corrector $d\mathbf{u}$. Substituting the relation $\Delta \mathbf{u}^{i+1} = \Delta \mathbf{u}^i + d\mathbf{u}$ in Eq. (4) and expanding in the linearized weak form of Eq. (5) yields:

$$\int_{\Omega_C^t} \delta \mathbf{e}^t : \mathbb{C}^t : \Delta \mathbf{e}(d\mathbf{u}) d\Omega + \int_{\Omega_C^t} \delta \boldsymbol{\eta}^t : \boldsymbol{\sigma}^t d\Omega = -G^t(\Delta \mathbf{u}^i, \delta \mathbf{u}) \quad (6)$$

where

$$\delta \mathbf{e}^t = \frac{1}{2} \left[\left(\frac{\partial \delta \mathbf{u}}{\partial \mathbf{x}^t} \right)^T + \frac{\partial \delta \mathbf{u}}{\partial \mathbf{x}^t} \right] \quad (7a)$$

$$\delta \boldsymbol{\eta}^t = \frac{1}{2} \left[\left(\frac{\partial \delta \mathbf{u}}{\partial \mathbf{x}^t} \right)^T \frac{\partial \mathbf{u}}{\partial \mathbf{x}^t} + \left(\frac{\partial \mathbf{u}}{\partial \mathbf{x}^t} \right)^T \frac{\partial \delta \mathbf{u}}{\partial \mathbf{x}^t} \right] \quad \text{and} \quad (7b)$$

$$-G^t(\Delta \mathbf{u}^i, \delta \mathbf{u}) = W R_{ext}^{t+\Delta t} - \int_{\Omega_C^t} \delta \mathbf{e}^t : \mathbb{C}^t : \Delta \mathbf{E}^t(\Delta \mathbf{u}^i) d\Omega_C^t - \int_{\Omega_C^t} \delta \boldsymbol{\eta}^t : \mathbb{C}^t : \Delta \mathbf{E}^t(\Delta \mathbf{u}^i) d\Omega_C^t - \int_{\Omega_C^t} \delta \mathbf{e}^t : \boldsymbol{\sigma}^t d\Omega_C^t - \int_{\Omega_C^t} \delta \boldsymbol{\eta}^t : \boldsymbol{\sigma}^t d\Omega_C^t \quad (7c)$$

For the i th iteration in the modified Newton–Raphson algorithm, the corresponding matrix equation can be derived from the linearized equation (6) as:

$$\mathbf{K}_t^i d\mathbf{u}^i = \mathbf{R}_{ext}^{t+\Delta t} - \mathbf{R}^i = \hat{\mathbf{R}}^i \quad (8)$$

where $\mathbf{R}_{ext}^{t+\Delta t}$ is the external load vector, \mathbf{R}^i is the internal load vector, $\hat{\mathbf{R}}^i$ is the residual force vector and $d\mathbf{u}^i$ is the correction to the displacement increment in the i th iteration. The global stiffness matrix \mathbf{K}_t^i is obtained by global assembly of element matrices, expressed as:

$$(\mathbf{K}_t^e)^i = \left[\int_{\Omega_e^t} \mathbf{B}^T \mathbb{C}^t \mathbf{B} d\Omega + \int_{\Omega_e^t} \mathbf{B}_{NL}^T \boldsymbol{\sigma}^t \mathbf{B}_{NL} d\Omega \right] \quad (9)$$

where \mathbf{B} and \mathbf{B}_{NL} are the linear and nonlinear strain–displacement matrices for an element e respectively, for that iteration. The elastic–plastic tangent stiffness matrix \mathbb{C}^t for the crystal plasticity model in Section 3 is derived from Appendix. The modified Newton–Raphson iterations continue till the residual $\hat{\mathbf{R}}^i$ reaches a predetermined tolerance.

2.2. Molecular dynamics solution of the atomistic domain

The position of atoms in the atomistic domain Ω_A is evaluated by performing MD simulations using the *Large-scale Atomic/Molecular Massively Parallel Simulator* LAMMPS [28], along with a time acceleration scheme discussed in Section 4. The MD simulations are governed by the equation of motion:

$$m_p \ddot{\mathbf{r}}_p = \mathbf{f}_p \quad \forall \mathbf{r}_p \in \Omega_A \quad (10)$$

where m_p , \mathbf{r}_p and $\ddot{\mathbf{r}}_p$ are the mass, position and acceleration of an atom p subjected to a force vector \mathbf{f}_p . The velocity-Verlet time integration scheme is used to numerically integrate equation (10) in the LAMMPS code. \mathbf{f}_p has contributions from different sources of interaction from atoms in Ω_A , depending on the sub-region that the atom is located in. A detailed discussion of the construction of \mathbf{f}_p is given in Section 4.

2.3. Kinematic compatibility and traction reciprocity constraints in the interface domain Ω_I

For each load increment on the traction boundary Γ_σ^t , the FE equation (8) for the continuum domain Ω_C is solved by enforcing a compatibility constraint in the interface domain Ω_I , expressed as:

$$\Delta \mathbf{u}_\beta^C = \frac{1}{N_\beta} \sum_{p \in G_\beta} \Delta \mathbf{u}_p^A \quad \forall \beta \in \Omega_I \quad (11)$$

where \mathbf{u}_β^C is the displacement of an interface FE node β , and $\mathbf{u}_p^A (= \mathbf{r}_p - \mathbf{r}_p^0)$ is the displacement of an atom p . The weighting function $\frac{1}{N_\beta}$ corresponds to the contribution of an atom p in the Voronoi cell G_β to the weighted-averaged atomic displacement, where N_β is the total number of atoms in G_β .

Traction reciprocity between the continuum and atomistic domains is enforced in Ω_I by applying forces on the interface atoms that are consistent with nodal tractions in the continuum domain. The traction for an interface node β can be extracted from the global internal force vector \mathbf{R}_t^β in Eq. (8). The interfacial traction force on each atom p belonging to the cluster of atoms in the associated Voronoi cell G_β is computed by equidistributing the force for the interface node β as:

$$\mathbf{f}_p^{\text{ext}} = \frac{1}{N_\beta} \mathbf{R}_t^\beta \quad (12)$$

where N_β is the total number of atoms in G_β .

Solving for the displacement increments in the time interval $t \rightarrow t + \Delta t$ involves the following steps.

1. For iteration loop i in the modified Newton–Raphson solution method, establish the global stiffness matrix \mathbf{K}_t^i using Eq. (9) for the domain Ω_C .
2. Enforce the displacement compatibility constraint condition (11) across domains in the interface region Ω_I .
3. Iteratively solve equation (8) to obtain the updated displacement fields in Ω_C .
4. Apply the traction reciprocity condition (12) to atoms in the interface domain Ω_I .
5. Update atomic positions by solving equation (10) with the velocity-Verlet time integration method.
6. Check for convergence in the interface displacement solution.

A flowchart, delineating the details of the solution procedure, is given in Fig. 12.

3. Dislocation density-based crystal plasticity model for Ω_C

The continuum domain Ω_C for pure Ni single crystals is modeled using a dislocation density-based crystal plasticity material model discussed in [21,22]. For finite deformation, the deformation modes include elastic stretching, crystal lattice rotation and plastic slip. The deformation gradient \mathbf{F} admits a multiplicative decomposition into elastic and plastic components, given as:

$$\mathbf{F} = \mathbf{F}^e \mathbf{F}^p \quad \text{where} \quad \det \mathbf{F}^e > 0 \quad \text{and} \quad \det(\mathbf{F}^p) = 1 \quad (13)$$

The elastic part of the deformation gradient \mathbf{F}^e incorporates both lattice rotation and elastic stretch through the relation $\mathbf{F}^e = \mathbf{R}^e \mathbf{U}^e$. The rates of the elastic and plastic components of the deformation gradient are given as:

$$\dot{\mathbf{F}}^e = \mathbf{L} \mathbf{F}^e - \mathbf{F}^e \mathbf{L}^p \quad \text{and} \quad \dot{\mathbf{F}}^p = \mathbf{L}^p \mathbf{F}^p \quad (14)$$

where $\mathbf{L} = \dot{\mathbf{F}} \mathbf{F}^{-1}$ and $\mathbf{L}^p = \dot{\mathbf{F}}^p \mathbf{F}^{p-1}$. For dislocation-mediated plasticity, the plastic velocity gradient \mathbf{L}^p is expressed in terms of the plastic shear-rate $\dot{\gamma}^\alpha$ on slip system α as:

$$\mathbf{L}^p = \dot{\mathbf{F}}^p \mathbf{F}^{p-1} = \sum_{\alpha=1}^N \dot{\gamma}^\alpha \mathbf{m}_0^\alpha \otimes \mathbf{n}_0^\alpha = \sum_{\alpha=1}^N \dot{\gamma}^\alpha \mathbf{s}_0^\alpha \quad (15)$$

The Schmid tensor is expressed as $\mathbf{s}_0^\alpha \stackrel{\text{def}}{=} \mathbf{m}_0^\alpha \otimes \mathbf{n}_0^\alpha$, where \mathbf{m}_0^α and \mathbf{n}_0^α are respectively the slip direction and slip plane normal in the reference configuration. The FCC crystal structure has three slip planes that are represented by slip plane normals \mathbf{m}_0^α , with each slip plane having three slip directions represented by \mathbf{n}_0^α .

The stress–strain relation is expressed in an elastically deformed reference configuration, in terms of the second Piola–Kirchhoff stress $\hat{\mathbf{S}}$ and the elastic Green–Lagrange strain \mathbf{E}^e , as:

$$\hat{\mathbf{S}} = \mathbb{C}^e : \mathbf{E}^e \quad (16)$$

where \mathbb{C}^e is a fourth-order anisotropic elasticity tensor in the material symmetry coordinates. The second Piola–Kirchhoff stress $\hat{\mathbf{S}}$ and the Green–Lagrange strain tensor \mathbf{E}^e are respectively defined as:

$$\hat{\mathbf{S}} \equiv \det(\mathbf{F}^e) \mathbf{F}^{e^{-1}} \boldsymbol{\sigma} \mathbf{F}^{e^{-T}} \text{ and } \mathbf{E}^e \equiv \frac{1}{2} (\mathbf{F}^{eT} \mathbf{F}^e - \mathbf{I}) \quad (17)$$

where \mathbf{I} is the identity tensor and $\boldsymbol{\sigma}$ is the Cauchy stress tensor.

The plastic shearing-rate $\dot{\gamma}^\alpha$, calculated from the Orowan equation [31], has contributions from two types of dislocations. One is due to the evolution of pre-existing statistically stored dislocations (SSDs), while the other is due to free glide of dislocations nucleating from the crack-tip. Accordingly, the plastic shearing-rate is written as:

$$\dot{\gamma}^\alpha = \dot{\gamma}^\alpha|_{SSD} + \dot{\gamma}^\alpha|_{nuc} \quad (18)$$

where the shearing-rate due to the pre-existing SSDs is given as:

$$\dot{\gamma}^\alpha|_{SSD} = \rho_{mSSD}^\alpha b v^\alpha \quad (19)$$

ρ_{mSSD}^α is the mobile part of the SSD density, b is the magnitude of the Burgers vector, and v^α is the dislocation velocity on the slip system α given in Eq. (21). The shearing-rate in the slip system α due to free glide of nucleated dislocations is expressed as:

$$\dot{\gamma}^\alpha|_{nuc} = \rho_{mnuc}^\alpha b v^\alpha \quad (20)$$

where ρ_{mnuc}^α is the mobile part of nucleated dislocations.

3.1. A unified slip system dislocation velocity for the orowan equation

The concurrent model contains different types of dislocations that depend on its neighborhood dislocation structure. These include those in the dislocation cell structure, located far from the crack tip, as well as stand-alone dislocations near the crack tip. The velocity of a dislocation is determined by the local stress state and the resistance encountered due to the presence of barriers in the form of forest and parallel dislocations [22]. The critical resolved shear stress (CRSS) τ_C , which is a measure of the barrier strength to be overcome for dislocation glide, is high $\sim O(10^2 \text{ MPa})$ away from the crack tip. At these locations, the resolved shear stress is low compared to those near the crack tip location. This results in a low dislocation velocity. On the other hand, dislocations nucleated from the crack-tip experience a very high resolved shear stress owing to their proximity to the crack tip. This region is also free from pre-existing dislocations and has low $\tau_C \sim O(10 \text{ MPa})$ primarily due to lattice friction. Consequently, the velocity of nucleated dislocations is high. The propagation speed of these dislocations, immediately after nucleation, can reach the material shear-wave speed $v_\infty = \sqrt{G/\rho}$, where G and ρ are respectively the shear modulus and density. To represent these velocities as limiting cases, a unified form of dislocation velocity is expressed using an exponential form as:

$$v^\alpha = \lambda_1 v_\infty \left[\frac{\exp\left(-\frac{Q_{act}}{k_B \theta}\right)}{1 + \lambda_2 \exp\left(-\frac{\langle \tau^\alpha - \tau_{pass} \rangle}{\tau_{cut}}\right)} \right] \text{sgn}(\tau^\alpha) \quad (21)$$

where v_∞ is the upper bound of the dislocation velocity, corresponding to the shear-wave speed. Q_{act} is the activation energy required for a dislocation to overcome the local barrier without the aid of any applied shear stress, k_B is the Stefan–Boltzmann constant and θ is the absolute temperature in Kelvin. $\langle \bullet \rangle$ is the Macaulay bracket and $\text{sgn}(\bullet)$ is the sign-function. λ_1 and λ_2 are material constants that are calibrated from MD simulation results to obtain the velocity of a single dislocation under different driving shear stresses. The parameter λ_1 controls the maximum

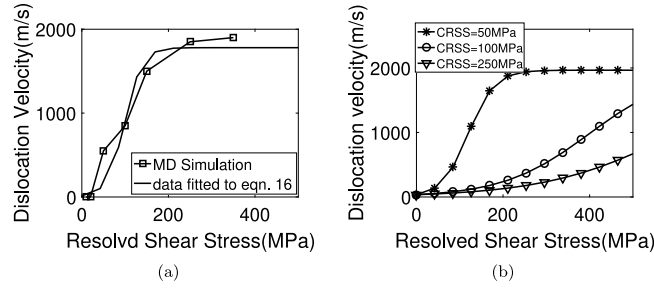


Fig. 3. Dislocation velocity as a function of the resolved shear stress for a pure Ni single crystal: (a) velocity of a free gliding dislocation fitted to the functional form of Eq. (21), and (b) velocity profile of a dislocation gliding through pre-existing dislocations, represented by a higher τ_C value.

dislocation velocity. Though the theoretical sound wave speed for pure Ni ($G = 125$ GPa and $\rho = 8908$ Kg/m³) is calculated to be $\sqrt{G/\rho} = 3746$ m/s, the maximum velocity of dislocation has been observed to be ~ 2000 m/s in [32]. τ_α is the resolved shear stress on the slip system α , and τ_{pass} and τ_{cut} are the passing and cutting stresses respectively.

Fig. 3(a) shows dislocation velocities due to different applied shear stresses. The CRSS τ_C for dislocation glide in pure Ni single crystal is found to be ~ 10 MPa. The dislocation velocity reaches a stable magnitude of 1900 m/s within an applied shear stress of 200MPa. A similar finding has been reported in [33]. Velocity data from MD simulations are used to obtain the control parameters as: $\lambda_1 = 1.3$ and $\lambda_2 = 51.2$. For these evaluations, it is assumed that $\tau_{pass} = \tau_{cut} = \tau_C$ and $Q_{act} \approx 1k_B\theta$. Fig. 3(b) shows the velocity profile of a dislocation for different values of τ_C . A low τ_C value $\sim O(10$ MPa) implies glide through a perfect crystal, while the larger τ_C values $\sim O(100$ MPa) may be related to the dislocation velocity passing through denser dislocation cell structures.

3.2. Resolved shear stress components and mobile dislocation densities

The passing stress τ_{pass}^α in Eq. (21) represents the resistance to dislocation glide in the presence of other dislocations in the same slip plane, while the cutting stress τ_{cut}^α corresponds to the resistance in the presence of other dislocations perpendicular to the slip plane. These stresses are respectively expressed as:

$$\begin{aligned}\tau_{pass}^\alpha &= c_1 G b \sqrt{\rho_P^\alpha + \rho_{mSSD}^\alpha + \rho_{mnucl}^\alpha} \\ \tau_{cut}^\alpha &= \frac{Q_{act} \sqrt{\rho_F^\alpha}}{c_2 b^2}\end{aligned}\quad (22)$$

where c_1 and c_2 are material constants.

Plastic flow in the continuum region is considered to be dominated by statistically stored dislocations (SSDs) and localized geometrically necessary dislocations (GNDs) near the crack tip. The rate of evolution of SSD density has four major components due to (i) lock formation ($\dot{\rho}_{SSDlf}^{\alpha+}$), (ii) dipole formation $\dot{\rho}_{SSDdf}^{\alpha+}$, (iii) athermal annihilation $\dot{\rho}_{SSDaa}^{\alpha-}$ and (iv) thermal annihilation $\dot{\rho}_{SSDta}^{\alpha-}$, i.e.,

$$\dot{\rho}_{SSD}^\alpha = \dot{\rho}_{SSDlf}^{\alpha+} + \dot{\rho}_{SSDdf}^{\alpha+} + \dot{\rho}_{SSDaa}^{\alpha-} + \dot{\rho}_{SSDta}^{\alpha-}\quad (23)$$

The superscripts $+/-$ correspond to whether the contributing term is multiplication or annihilation of dislocations. Their rates are given in [21,22] as:

$$\begin{aligned}\dot{\rho}_{SSDlf}^{\alpha+} &= \frac{c_3}{b} \sqrt{\rho_F^\alpha} \dot{\gamma}_{SSD}^\alpha \\ \dot{\rho}_{SSDdf}^{\alpha+} &= \frac{c_4}{b} \frac{\sqrt{3} G b}{16\pi(1-\nu)} (|\tau^\alpha| - \tau_{pass}^\alpha)^{-1} \rho_{mSSD}^\alpha \dot{\gamma}_{SSD}^\alpha \\ \dot{\rho}_{SSDaa}^{\alpha-} &= -c_5 \rho_{SSD}^\alpha \dot{\gamma}_{SSD}^\alpha \\ \dot{\rho}_{SSDta}^{\alpha-} &= -c_6 \frac{D_0 b^3}{k_B \theta} \exp\left(\frac{-Q_{act}}{k_B \theta}\right) (\rho_{SSD}^\alpha)^2 |\tau^\alpha| \left(\frac{\dot{\gamma}_{SSD}^\alpha}{\dot{\gamma}_{ref}^\alpha}\right)^{c_7}\end{aligned}\quad (24)$$

For computing the mobile dislocation density ρ_m^α , the SSD density is projected into a forest dislocation density ρ_F^α and a parallel dislocation density ρ_P^α , with interaction strength coefficients $\chi^{\alpha\beta}$ between the different slip systems [22], as:

$$\begin{aligned}\rho_F^\alpha &= \sum_{\beta=1}^N \chi^{\alpha\beta} \left[\rho_{SSD}^\beta |\cos(\mathbf{n}^\alpha, \mathbf{t}^\beta)| \right] \\ \rho_P^\alpha &= \sum_{\beta=1}^N \chi^{\alpha\beta} \left[\rho_{SSD}^\beta |\sin(\mathbf{n}^\alpha, \mathbf{t}^\beta)| \right]\end{aligned}\quad (25)$$

The mobile dislocation density is subsequently computed as [21,22]:

$$\rho_{mSSD}^\alpha = \frac{2k_B\theta\sqrt{\rho_F^\alpha\rho_P^\alpha}}{c_1c_2Gb^3}\quad (26)$$

The other contributor to the mobile dislocation density viz. GNDs, occurs in regions of high stress-gradients to preserve lattice continuity [34]. The region of high stress gradient is in the vicinity of the crack tip, which is modeled using MD with an atomistic resolution. Correspondingly, the GNDs necessary to maintain lattice continuity in this region are naturally nucleated from the crack tip. All dislocations that nucleate from the crack tip in the atomistic region Ω_A and enter the crystal plasticity region Ω_C through the interface Ω_I are consequently considered as GNDs. The propagation/transport of these dislocations in the continuum domain is modeled using an advection model, expressed as:

$$\dot{\rho}_{nucl}^\alpha + \nabla \cdot (\rho_{nucl}^\alpha \mathbf{v}^\alpha) = \rho_s\quad (27)$$

where ∇ is the gradient operator and \mathbf{v}^α is the dislocation velocity vector in Eq. (21). The source term ρ_s corresponds to the generation of new dislocation density in Ω_C due to the influx of dislocations from the atomistic region Ω_A through the interface Ω_I . This is discussed in Section 5. Unlike SSDs, the GND density is not decomposed into forest and parallel densities as it directly contributes to the plastic shear-rate in Eq. (20). The crack tip-nucleated dislocations propagate through a dislocation free zone before interacting with other dislocations, and hence it is more appropriate to consider GNDs as mobile i.e. $\rho_{mnucl}^\alpha = \rho_{nucl}^\alpha$. The advection equation has been previously used to model the propagation of dislocations within continuum crystal plasticity model, e.g. in [35,36]. A major difference of the present work with these references is in the construction of the source term ρ_s and the dislocation velocity profile \mathbf{v}^α in Eq. (27) from atomic-scale MD simulations.

3.2.1. Subdomains of the continuum domain Ω_C

The presence of a crack in the concurrent model creates a localized region, which is initially free of dislocations. The initial dislocation-free region comprises the entire atomistic domain Ω_A and only a part of the continuum domain Ω_C of the coupled model. The continuum region is consequently divided into three subdomains that depend on the distribution of the initial dislocation density, as shown in Fig. 4(a).

1. Subdomain of no dislocation density (NDD) or Ω_C^{NDD} , corresponding to the innermost part of the continuum domain that does not contain any initial dislocation.
2. Subdomain of graded dislocation density (GDD) or Ω_C^{GDD} , is an annular region adjacent to Ω_C^{NDD} , where initial dislocation density is graded from 0 to ρ_{init}^{max} . ρ_{init}^{max} is the maximum initial dislocation density that the material contains if there were no cracks present.
3. Subdomain of constant dislocation density (CDD) or Ω_C^{CDD} , corresponding to the rest of continuum region that contains a uniform initial dislocation density of ρ_{init}^{max} .

The magnitude of ρ_{init}^{max} and the dimensions of the subdomains Ω_C^{NDD} , Ω_C^{GDD} and Ω_C^{CDD} depend on the material being modeled and the crack dimensions.

4. Time-accelerated molecular dynamics (MD) model for the atomistic domain

A strain-boost hyperdynamics algorithm, developed in [37,38] for temporal acceleration of MD simulations with the LAMMPS code [28], is implemented in this work. This algorithm has been incorporated in the concurrent framework for brittle fracture of Ni single crystal at lower strain-rates in [15,39]. The atomistic domain Ω_A is divided in four sub-domains based on the type of forces that the atoms in that region are subjected to. They are:

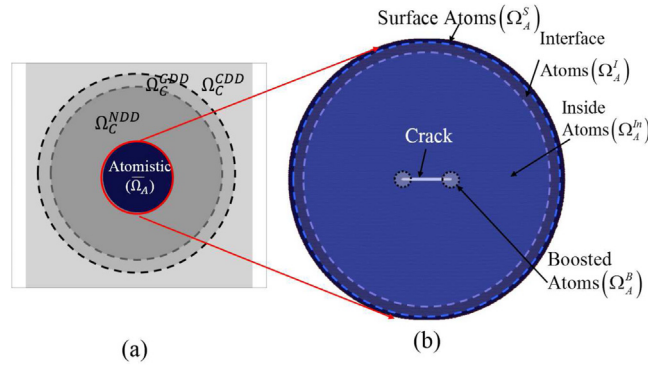


Fig. 4. Different subdomains belonging to the concurrent atomistic–continuum computational domain: (a) the continuum domain showing subdomains Ω_C^{NDD} , Ω_C^{GDD} and Ω_C^{DDD} , and (b) zoomed-in view of the atomistic region with a crack delineating subdomains Ω_A^{In} , Ω_A^I , Ω_A^S and Ω_A^B .

1. Subdomain Ω_A^{In} of atoms, whose motion is governed by interactions with neighboring atoms only. The interatomic interaction is represented by the many-body *embedded atom model* (EAM) potential [40]. The EAM potentials Φ are appropriate for modeling metallic materials, where electrons are spread more like a cloud, contrary to the covalent bond structure. The corresponding force experienced by atoms is computed as:

$$\mathbf{f}_p^{In} = -\nabla \Phi \quad (28)$$

2. Subdomain Ω_A^I of atoms belonging to the interface region. In addition to interatomic interactions, these atoms experience forces due to their interaction with the associated FE node. Damping is also applied to this region for maintaining a fixed temperature and elastic waves are suppressed by using a Langevin thermostat [41]. The force experienced by these atoms is computed as:

$$\mathbf{f}_p^I = -\nabla \Phi + \mathbf{f}_p^{ext} - \gamma m_p \dot{\mathbf{r}}_p + \sqrt{2\gamma K_B \theta m_p} R(t) \quad (29)$$

where γ is the damping coefficient, k_B is the Stefan–Boltzmann constant, θ is the target temperature and $R(t)$ is a δ -correlated stationary Gaussian process with zero-mean value, where δ is the delta function.

3. Subdomain Ω_A^S of atoms belonging to the surface region. Ghost force corrections are made over atoms in this region to mitigate the free surface effect [13–15]. The corresponding forces are given as:

$$\mathbf{f}_p^S = -\nabla \Phi - \mathbf{f}_p^G - \gamma m_p \dot{\mathbf{r}}_p + \sqrt{2\gamma K_B \theta m_p} R(t) \quad (30)$$

where \mathbf{f}_p^G is the mitigating force for the free surface effect.

4. Subdomain Ω_A^B of atoms that form the crack tip and contribute to the nucleation of dislocations. To accelerate the nucleation process in this region, the atoms are modeled with the strain-boost hyperdynamics accelerated MD [37,42]. These atoms experience an additional force due to the applied boost potential given as,

$$\mathbf{f}_p^B = -\nabla \Phi - \nabla \{\Delta V(r)\} \quad (31)$$

where $\Delta V(r)$ is the boost potential developed in [15,38]. Fig. 4 shows the details of all the different subdomains of the atomistic region Ω_A .

4.1. Bridging time scales between the atomistic and continuum domains

Asynchronous response of the atomistic and continuum domains in the concurrent model renders the two domains to experience different deformation rates. The velocity-Verlet time integration in MD simulations requires very small time steps $\Delta t_{MD} \sim 1$ fs from stability considerations. The corresponding applied strain-rates are significantly high ($\dot{\epsilon} \sim 1.0e8$) [43]. To overcome difficulties with this time-scale mismatch, a strain-boost hyperdynamics time-acceleration method has been developed in [15] for MD simulations in the concurrent model. This method is used in the present study to match the time scales of the atomistic and continuum domains.

5. Domain transfer of nucleated dislocations with transformation at the interface

The evolution of plasticity in the concurrent model requires special consideration of dislocation transfer and transformation. Dislocations nucleate from the crack tip in Ω_A , signaling an onset of plasticity. Due to a large negative stress-gradients in the neighborhood of the crack tip, the nucleated dislocations propagate through the atomistic region and approach the interface Ω_I . Upon reaching Ω_I , the discrete dislocations in the atomistic domain should undergo an appropriate transformation for manifestation as dislocation densities in the continuum domain Ω_C . The transformation requires establishing the equivalence between the total dislocation length and the dislocation density gradient in the dislocation core. The transformation method should be valid for any kind of dislocation, e.g. straight or curved dislocation. Once in the continuum domain, the transformed dislocation densities will propagate at a velocity given in Eq. (21), based on the local resolved shear stress τ^α for the slip system. The propagation continues till they reach a region where the propagation velocity of the nucleated dislocations is drastically reduced, due to interaction with pre-existing SSDs.

5.1. Identification of discrete dislocations from lattice configurations

Prior to transfer and transformation at the interface Ω_I , dislocations are characterized and quantified using the dislocation extraction algorithm (DXA) [25]. For a given atomic configuration, the DXA first separates atoms that are not in perfect lattice configuration from those that are in perfect lattice configuration. For this purpose, an atomic structure identification algorithm such as the common neighbor analysis (CNA) [44] is used. Once the atoms that form a defect structure like the dislocation core are identified, the Burger circuit method is used to track down the dislocation and represent it as a collection of points known as dislocation beads. Fig. 5 depicts the steps involved in extracting dislocations from a given atomic configuration using the DXA. The distance between each consecutive pair of beads is considered as a dislocation line segment $d\mathbf{l}$. Fig. 5(d) shows an example of this representation with dislocation beads and line segments.

5.2. Transforming dislocations from discrete to field forms

The length of each line segment is the Euclidean distance between the beads it consists of. For transforming dislocations from their discrete representation to the density field manifestation, it is necessary to convert the dislocation line lengths $\|d\mathbf{l}\|$ into a line density form. A Gaussian distribution function is assumed for this transformation. This distribution function at any location \mathbf{x} can be written as:

$$w(\mathbf{x}, \mathbf{X}) = \frac{1}{(\sigma\sqrt{2\pi})^3} e^{-\frac{(\|\mathbf{x}-\mathbf{X}\|)^2}{2\sigma^2}} \quad (32)$$

where \mathbf{X} is the position vector of a dislocation segment in the discrete form and $\|\bullet\|$ is the 3D Euclidean distance. The vector \mathbf{X} for the dislocation segment $d\mathbf{l}$ is approximated by the position vector of the midpoint of the bead-pair that define the segment. The symbol σ corresponds to the standard deviation of the Gaussian distribution, representing the spread of the dislocation density. It can be estimated by analyzing the stress field around a dislocation. This stress field can be obtained from the Volterra construction discussed in [45]. Two types of dislocations are considered, viz. the straight-edge and straight-screw dislocations. Any dislocation of mixed character can always be decomposed into an edge component and screw component and the stress field can be obtained by superposing the stress fields for the individual components. Fig. 6 shows the contour plot of the stress field around a straight dislocation.

To obtain a material independent estimate of the stress field, the magnitude of the normal stresses is normalized by the Young's modulus, and the shear stresses by the shear modulus of the material respectively. Spatial dimensions are also normalized by the magnitude of Burgers vector $\|\vec{b}\|$. It is observed that for both edge and screw dislocations, the dominant normalized stress component reduces to less than 5% beyond a spatial distance of $5\|\vec{b}\|$ from the dislocation core. For the Gaussian distribution, 95% of the density lies within the 2σ distance from the mean. Correspondingly, the standard deviation σ is evaluated from the spatial distance, beyond which the normalized stress reduces to 5% or less. Hence the standard deviation is taken as $\sigma = 2.5\|\vec{b}\|$. For pure Ni with $\|\vec{b}\| \approx 2.49\text{\AA}$, the value of $\sigma \approx 6.25\text{\AA}$. For mixed dislocations, the Burgers vector can be evaluated from projection on to edge and screw components. Since the non-zero stress components σ_{xx} , σ_{yy} and σ_{xy} due to edge dislocation, and stress

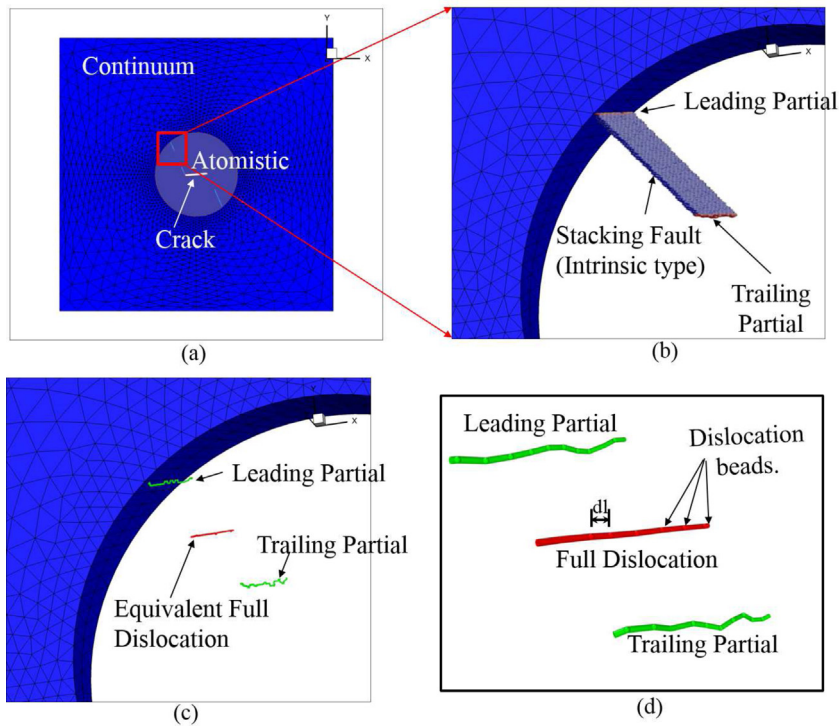


Fig. 5. Steps involved in the extraction of dislocations from a given atomic configuration: (a) concurrent model with dislocations in the atomistic region, (b) dislocations and stacking faults identified by using CNA (red atoms represent the core of the leading and trailing partial dislocations, while blue atoms represent the stacking fault between two partials), (c) dislocations converted from atomic representation to the discrete form, and (d) smoothed out extracted dislocations, mitigating noise due to thermal vibration. (For interpretation of the references to color in this figure legend, the reader is referred to the web version of this article.)

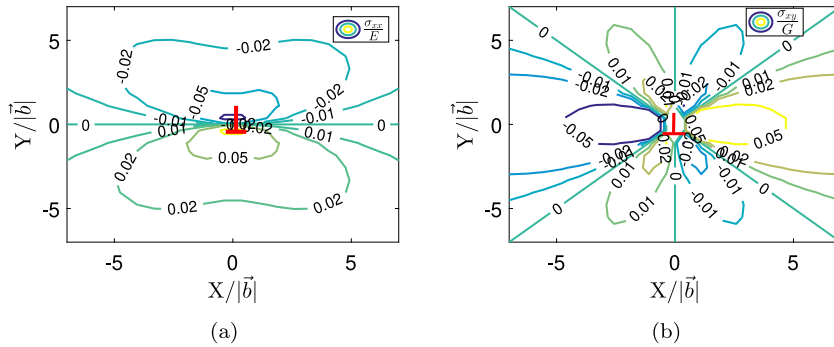


Fig. 6. Contour plot of the stress in the presence of an edge dislocation: (a) σ_{xx} and (b) σ_{xy} .

components σ_{xz} and σ_{yz} due to screw dislocation are mutually exclusive, similar decay is also expected for mixed dislocations. Thus for mixed dislocations also, the normalized stress is expected to reduce below 5% beyond a spatial distance of $5\|\vec{b}\|$ from the dislocation core. Figs. 6(a) and 6(b) show the contour plots of σ_{xx} and σ_{xy} for a straight-edge dislocation respectively. The figures show that both the normalized stress components reduce to less than 5% beyond a spatial distance of $5\|\vec{b}\|$ from the dislocation core.

With the Gaussian distribution function given in Eq. (32), the dislocation density at a location with position vector \mathbf{x} is expressed as:

$$\rho_{nuc}(\mathbf{x}) = w(\mathbf{x}, \mathbf{X}) \|\mathbf{dl}\| \quad (33)$$

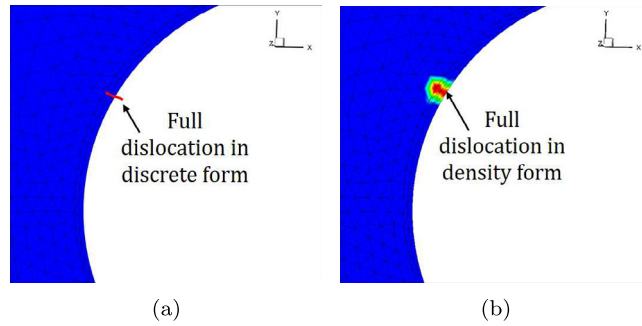


Fig. 7. Transformation of a dislocation at the interface from its (a) discrete representation in the atomistic domain Ω_A^I to the (b) dislocation density representation in the continuum domain Ω_C^I .

where $\|\mathbf{dl}\|$ is the length of the dislocation segment and $\rho_{nucl}(\mathbf{x})$ is the dislocation density at \mathbf{x} . Since $\int_{\Omega} w(\mathbf{x}, \mathbf{X}) = 1$, the integral of the nucleated dislocation density $\int_{\Omega} \rho_{nucl}(\mathbf{x}) = \|\mathbf{dl}\|$. This implies that the total dislocation length is preserved in the dislocation transformation from the discrete to density form. In the coupled concurrent model, the dislocations are identified in the dislocation detection zone Ω_{DD} . Fig. 7 shows one such dislocation transformation at the interface from discrete representation in the atomistic domain Ω_A^I to a density representation in the continuum domain Ω_C^I .

6. Propagating the transformed dislocation density field in Ω_C

Propagation of the dislocation density field in the continuum domain is modeled using the transport equation of a conserved quantity without dispersion, also known as the advection equation. For a conserved scalar quantity, like the dislocation density ρ , the advection equation is written as:

$$\frac{\partial \rho}{\partial t} + \nabla \cdot (\rho \mathbf{v}) = \frac{\partial \rho}{\partial t} + \mathbf{v} \cdot \nabla \rho + \rho \nabla \cdot \mathbf{v} = \rho_s \quad (34)$$

where ∇ is the gradient operator, \mathbf{v} is the velocity field of ρ and ρ_s is a source term that represents dislocation density generation due to: (i) incoming dislocations from the atomistic region, and (ii) the expansion of the dislocation loop. On account of the specific orientation of the crystal structure resulting in straight dislocations, the source term ρ_s mainly represents the density due to incoming dislocations from the atomistic region. The spatial length-scale over which dislocation density ρ varies is $\sim \|\vec{b}\| \sim 1.0e-10$ m, where $\|\vec{b}\|$ is the magnitude of the Burgers vector. On the other hand, the dislocation velocity \mathbf{v} varies over a length-scale $\sim 1.0e-7$ m. The spatial gradient of ρ is at least three orders of magnitude higher than the spatial gradient of \mathbf{v} . Consequently, the term $\rho \nabla \cdot \mathbf{v}$ in Eq. (34) is ignored, yield the equation:

$$\frac{\partial \rho}{\partial t} + \mathbf{v} \cdot \nabla \rho = \rho_s \quad (35)$$

This equation should be numerically solved over the continuum domain for the dislocation-density propagation. It has already been seen in Section 5.1 that for an individual dislocation the core is spread over a spatial dimension, not exceeding $10\|\vec{b}\|$, which is $\approx 25\text{\AA}$ for pure Ni. To maintain the characteristic sharp gradient of dislocation density in a very localized zone, the discretization size should be $\sim O(5\text{\AA})$, which is computationally prohibitive with a FE mesh. The generation of the initial fine mesh is not only computationally expensive but the storage of the elemental connectivity is memory intensive also. A mesh-free particle method is considered to be a suitable choice for the numerical solution of Eq. (35). The reproducing kernel particle method (RKPM) is used in this work, in conjunction with the point collocation method. Computing the RKPM kernel function, an exponential function in this study, is however extremely time intensive. To mitigate the computational cost, the kernel function is evaluated from a pre-computed look-up table.

6.1. The Reproducing Kernel Particle Method (RKPM)

The RKPM [26] is an augmented form of the smooth particle hydrodynamics (SPH) method proposed in [46]. Two major aspects of this method are: (i) the kernel approximation for interpolation and (ii) particle approximation for domain discretization. The function $f(\mathbf{x})$ at a point \mathbf{x} may be approximated as a convolution integral using a kernel function as:

$$f(\mathbf{x}) = \int_{\Omega} f(\mathbf{s})\delta(\mathbf{x} - \mathbf{s})d\mathbf{s} \quad (36)$$

where $\delta(\mathbf{x} - \mathbf{s})$ is the Dirac delta function. The non-smooth, singular function $\delta(\mathbf{x} - \mathbf{s})$ can be replaced by a smoothing kernel function $W(\mathbf{x} - \mathbf{s}, h)$ to yield:

$$f(\mathbf{x}) \simeq \int_{\Omega} f(\mathbf{s})W(\mathbf{x} - \mathbf{s}, h)d\mathbf{s} \quad (37)$$

where h is a smoothing length. Correspondingly, the gradient of $f(\mathbf{x})$ is approximated as [26]:

$$\nabla f(\mathbf{x}) \simeq - \int_{\Omega} f(\mathbf{s})\nabla W(\mathbf{x} - \mathbf{s}, h)d\mathbf{s} \quad (38)$$

In the SPH method, the entire domain is represented by a distribution of finite number of particles. With this particle approximation, the continuous integral in Eqs. (37) and (38) are expressed as discretize sums over all the particles in the domain as:

$$f(\mathbf{x}) \simeq \sum_{i=1}^{N_I} f(\mathbf{x}_i)W(\mathbf{x} - \mathbf{x}_i, h)\Delta\Omega_i \quad (39a)$$

$$\nabla f(\mathbf{x}) \simeq - \sum_{i=1}^{N_I} f(\mathbf{x}_i)\nabla W(\mathbf{x} - \mathbf{x}_i, h)\Delta\Omega_i \quad (39b)$$

where N_I is the number of particles belonging to a support domain of the kernel function and $\Delta\Omega_i$ is a weight associated with the i th particle. The weighted kernel function $W(\mathbf{x} - \mathbf{x}_i, h)\Delta\Omega_i$ corresponds to the shape function associated with the i th particle in the SPH method.

The SPH shape function however cannot accurately reproduce the function or its gradients for particles that are close to the domain boundary, due to a lack of compact support for the kernel function. To overcome this limitation, the reproducing kernel particle method (RKPM) has been proposed in [26,47], where the kernel $W(\mathbf{x} - \mathbf{s}, h)$ in Eq. (37) is augmented by a correction function $C(\mathbf{x}, \mathbf{s})$. The augmented form of the function is expressed as:

$$f^a(\mathbf{x}) \simeq \int_{\Omega} f(\mathbf{s})\overline{W}(\mathbf{x} - \mathbf{s}, h)d\Omega \quad (40)$$

where $\overline{W}(\mathbf{x} - \mathbf{s}, h) = C(\mathbf{x}, \mathbf{s})W(\mathbf{x} - \mathbf{s}, h)$ is the augmented kernel function. A polynomial function has been proposed for $C(\mathbf{x}, \mathbf{s})$ in [47], where the order of the polynomial is chosen from the highest order of derivative present in the governing differential equations. Since the highest derivative in the dislocation density advection equation (35) is 1, a linear polynomial $C(\mathbf{x}, \mathbf{s}) = c_0(\mathbf{x}) + c_1(\mathbf{x})(\mathbf{x} - \mathbf{s})$ is used as the correction function. The coefficients $c_0(\mathbf{x})$ and $c_1(\mathbf{x})$ are determined by satisfying the reproducing conditions of the function and its spatial gradients. Details of determining these coefficients and their derivatives are given in [26,47].

6.2. Numerical implementation of the dislocation density propagation relations

Numerical solution of the advection equation (35) for the evolving dislocation density field ρ is conducted with the RKPM in conjunction with a point collocation method. The point collocation method yields a discrete set of the advection equations by satisfying the governing differential equation at a set of discrete material points that are solved by the RKPM. In an incremental solution process, the discrete form of the differential equations for the i th particle and at a time t_{n+1} is written as:

$$\left(\frac{\partial \rho}{\partial t}\right)_i^{n+1} + (\mathbf{v} \cdot \nabla \rho)_i^{n+1} = (\rho_s)_i^{n+1} \quad (41)$$

Substituting Eq. (38) into Eq. (41), the discrete form reduces to:

$$\left(\frac{\partial \rho}{\partial t}\right)_i^{n+1} - (\mathbf{v})_i^{n+1} \cdot \int_{\Omega_i} \rho^{n+1} \nabla \bar{W}_i ds = (\rho_s)_i^{n+1} \quad (42)$$

where \bar{W}_i is the RKPM kernel function for the i th particle and Ω_i is the support domain of \bar{W}_i . Incorporating the discrete particle form of the integral in Eq. (39), Eq. (42) reduces to:

$$\left(\frac{\partial \rho}{\partial t}\right)_i^{n+1} - \mathbf{v}_i^{n+1} \cdot \sum_{j=1}^{N_i} \rho_j^{n+1} \nabla \bar{W}_i(\mathbf{x}_i - \mathbf{x}_j, h) \omega_j = (\rho_s)_i^{n+1} \quad (43)$$

Using a backward Euler difference operator for the time derivative reduces this equation to:

$$\left(\frac{\rho_i^{n+1} - \rho_i^n}{\Delta t}\right) - \mathbf{v}_i^{n+1} \cdot \sum_{j=1}^{N_i} \rho_j^{n+1} \nabla \bar{W}_i(\mathbf{x}_i - \mathbf{x}_j, h) \omega_j = (\rho_s)_i^{n+1} \quad (44)$$

where $\Delta t = t_{n+1} - t_n$ is the time increment. Rearranging this equation results in the dislocation density for the i th particle as:

$$\rho_i^{n+1} - \sum_{j=1}^{N_i} \mathbf{v}_i^{n+1} \cdot \nabla \bar{W}_i(\mathbf{x}_i - \mathbf{x}_j, h) \omega_j \Delta t \rho_j^{n+1} = \Delta t (\rho_s)_i^{n+1} + \rho_i^n \quad (45)$$

Assembling equation (45) for all particles provides a set of linear algebraic equations that are solved for the particle-wise dislocation densities.

6.2.1. Imposing boundary condition

In meshless methods, imposing the Dirichlet boundary conditions is a key issue that has received special attention. Unlike element based methods, interpolation functions for particle-based methods typically do not satisfy the Kronecker delta and partition of unity properties. To account for this, a new set of algebraic equations have been proposed in [47] for particles on the boundary, satisfying the specified boundary conditions. For a boundary particle i , Eq. (45) is modified as:

$$\sum_{j=1}^{N_i} \bar{W}_i(\mathbf{x}_i - \mathbf{x}_j, h) \omega_j \rho_j^{n+1} = [\rho_i^{n+1}]_{sp} \quad (46)$$

where $[\rho_i^{n+1}]_{sp}$ is the dislocation density specified for the particle i at time t_{n+1} .

6.2.2. Particle/node-based integration scheme

Computational efficiency of particle methods depend on the numerical integration technique being used. Alternative integration methods have been suggested e.g. in [26,48] for stable and efficient integration. In [47], it has been shown that incorporating the point collocation method in a nodal integration scheme retains the characteristics of a true meshless method. In this method, the integral of a function $f(x)$ over a domain Ω is approximated as:

$$\int_{\Omega} f(x) d\Omega \approx \sum_{i=1}^{N_i} f(x_i) \Delta \Omega_i \quad (47)$$

where N_i is the number of particles used in the representation of Ω and $\Delta \Omega_i$ is a weight (nodal volume) associated with the i th particle. The nodal volume for each particle/node is determined by Voronoi tessellation [29] of the nodal domain. An advantage of the RKPM is that any error in the nodal volume is automatically corrected during the computation of coefficients of the correction function due to the reproducing condition [47]. Hence, the error in integration of Eq. (47) is due to discretization only.

6.2.3. Stabilizing the reproducing kernel particle method

Both the SPH and the RKPM methods suffer from instabilities that depend on the type of PDE being solved [46]. Stability analysis in [49] has shown that instability can be reduced significantly by an appropriate choice of the smoothing length h for the kernel function in Eq. (40). For a stable solution, the ratio of the smoothing length to the inter-particle distance should be in the range $\sim 1.0 - 1.4$. This ratio is maintained to be 1.3 in this study.

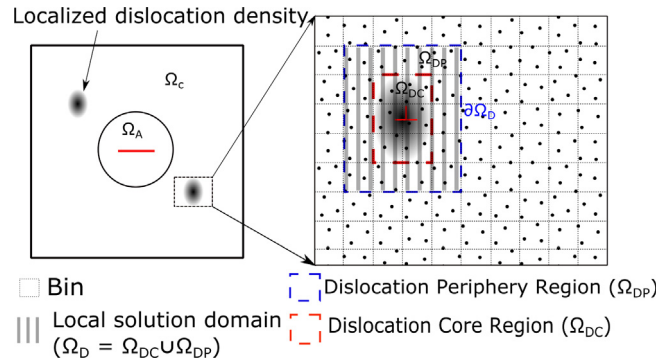


Fig. 8. Schematic representation of the local solution domain for the advection equation propagation of the nucleated dislocation density in the continuum domain Ω_C .

6.2.4. Improving computational efficiency through localized dislocation density solution

The dislocation core is localized in pockets of the continuum domain, with a length-scale $\sim O(10\|\vec{b}\|)$. Consequently, the nucleated dislocation density is concentrated in a few localized zones, while most of the continuum domain remains free of nucleated dislocations throughout the evolution process. This is shown in the schematic representation of Fig. 8. For improved computational efficiency, it is advantageous to restrict the solution of the dislocation evolution equation (35) to these localized regions of the computational domain. The local regions are identified by dividing the RKPM particle population into bins based on the dislocation density. The maximum dislocation density in each bin is computed at the end of each time step. The bins, for which the maximum dislocation density exceeds a threshold value, are assumed to contain the dislocation core Ω_{DC} . This is shown in Fig. 8. The dislocation core region Ω_{DC} along with its neighboring bins Ω_{DP} constitute the local solution domain i.e. $\Omega_D = \Omega_{DC} \cup \Omega_{DP}$, over which equation (35) is solved.

7. Developing the concurrent atomistic-crystal plasticity model

A major goal of the concurrent coupled model depicted in Fig. 10 is to study the influence of crack tip plasticity on crack evolution in crystalline metallic materials. The material investigated in this study is a pure Ni single crystal. The computational specimen consists of an embedded, through-thickness crack of initial length 20 nm in the xz -plane. The dimensions of the computational specimen are $200 \text{ nm} \times 200 \text{ nm} \times 4.22 \text{ nm}$. A cylindrical region Ω_C^{NDD} in Fig. 4 of radius 70 nm is considered to be free from initial dislocations. This dislocation-free region is followed by an annular region where the initial dislocation density is graded from 0 to $1.0e15 \text{ m}^{-2}$. The remaining exterior continuum region has a uniform initial dislocation density of $1.0e15 \text{ m}^{-2}$. The initial dislocation-free region gets populated with dislocations as the simulation progresses, and newly nucleated dislocations from the crack tip propagate into the continuum region.

7.1. Determining the computational domain size and dislocation-free zone

It has been experimentally observed in [50,51] that the presence of a micro-crack creates a localized dislocation-free zone in front of the crack tip. This dislocation-free zone mimics a perfect crystal, devoid of defects. To determine the overall size of the computational domain, it is necessary to estimate the approximate size of this dislocation-free zone. This can be assessed by analyzing the stress field in the presence of the crack, along with an estimate of the CRSS τ_C of the material due to pre-existing dislocations. The density of pre-existing dislocations in Ni has been determined to be of $O(10^{15})$ in [52]. With this dislocation density, the approximate passing stress τ_{pass}^α in Eq. (22) is computed to be $\approx 90 \text{ MPa}$. This value of τ_{pass}^α suffices as an estimate of τ_C . The resolved shear stress in the vicinity of the crack is expected to be much higher than the CRSS. This will cause the dislocations to move away from the crack tip, thus forming a localized dislocation-free zone.

The atomic configuration with a crack has been observed to nucleate dislocations at a volume-averaged stress of $\approx 3 \text{ GPa}$ in a previous study by the authors [38]. The size of the dislocation-free zone can be estimated from the

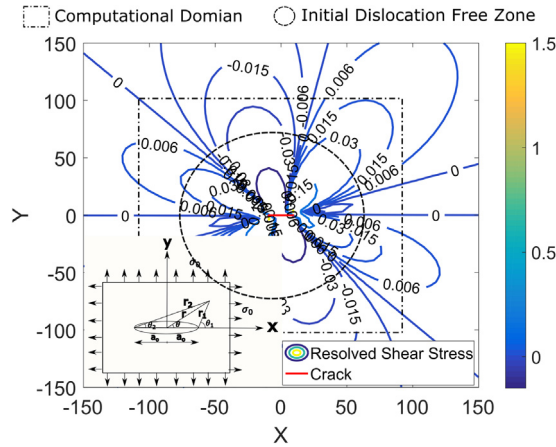


Fig. 9. The resolved shear stress (RSS) along the most critical slip system, from LEFM analysis. Spatial distances are in nm and stress are in GPa.

stress field in the presence of a crack with an externally applied biaxial loading of $\sigma_0 = 3$ GPa, which is analyzed using linear elastic fracture mechanics (LEFM). The stress field around a crack in an infinite plate due to an external far-field biaxial stress σ_0 has been derived in [53] using the Westergaard's solution as:

$$\begin{aligned}\sigma_{xx} &= \frac{\sigma_0 r}{\sqrt{r_1 r_2}} \left[\cos(\theta - \frac{1}{2}\theta_1 - \frac{1}{2}\theta_2) - \frac{\sigma_0 a_0^2}{(r_1 r_2)} r \sin \theta \sin \frac{3}{2}(\theta_1 + \theta_2) \right] \\ \sigma_{yy} &= \frac{\sigma_0 r}{\sqrt{r_1 r_2}} \left[\cos(\theta - \frac{1}{2}\theta_1 - \frac{1}{2}\theta_2) + \frac{\sigma_0 a_0^2}{(r_1 r_2)} r \sin \theta \sin \frac{3}{2}(\theta_1 + \theta_2) \right] \\ \sigma_{xy} &= \frac{\sigma_0 r}{\sqrt{r_1 r_2}} \left[\frac{a_0^2}{(r_1 r_2)} r \sin \theta \cos \frac{3}{2}(\theta_1 + \theta_2) \right]\end{aligned}\quad (48)$$

where $2a_0$ is the crack length, which is pre-determined to be $2a_0 = 20\text{nm}$. The other symbols in Eq. (48) have their conventional meaning and are also depicted in the inset of Fig. 9.

In the present study, the lattice orientation of the crystal with respect to the global axis is represented as: $x \rightarrow [11\bar{2}]$, $y \rightarrow [111]$ and $z \rightarrow [1\bar{1}0]$. The embedded crack has its tip located along the z -axis. For this specific orientation, the critical slip plane with the maximum RSS is inclined at an angle of 70.5° relative to the crack plane. To obtain the field of maximum RSS, the stress tensor obtained from Eq. (48) is transformed through a rotation of 70.5° . Fig. 9 shows a contour plot of the RSS on the most critical slip plane for a biaxial loading of $\sigma_0 = 3$ GPa. Beyond a cylindrical region with a radius of 70 nm, the RSS value drops below 90 MPa. Hence, a cylindrical region of radius 70 nm is considered as free from initial dislocations, corresponding to Ω_C^{NDD} in Fig. 4. The dislocation-free region is surrounded by an annular region, in which the initial dislocation density is gradually increased from 0 to 10^{15} m^{-2} . The outer shell of the continuum region contains a uniform initial dislocation density of 10^{15} m^{-2} . Dislocations nucleate from the crack tip and subsequently enter the initially dislocation-free region.

7.2. Minimum required size of the atomistic domain

The atomistic region in the concurrent model is computationally very expensive due to a large number of degrees of freedom ($\sim O(10^6)$). An optimal size of the atomistic region is therefore desirable for efficient solutions. This size can be estimated from the stretch of stacking faults. In FCC crystals, a full dislocation always splits into a leading partial and a trailing partial [45]. The leading partial nucleates first and is followed by the trailing partial. As the leading partial propagates through the crystal, it leaves behind a stacking fault, which is a localized HCP stacking in an otherwise FCC crystal. The trailing partial subsequently removes the stacking fault, thus restoring the perfect FCC crystal structure of the material. Since the continuum region is modeled by a dislocation density crystal plasticity model that incorporates full dislocations, it is necessary that both leading and trailing partials have

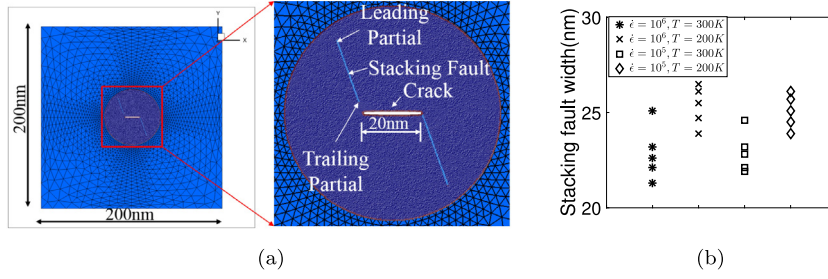


Fig. 10. Determining the size of the atomistic domain Ω_A by analyzing the stretch of the stacking fault: (a) the coupled model with a zoomed-in view of the atomistic domain, (b) variability of the maximum stretch of stacking fault for two strain-rates viz. $\dot{\epsilon} = 1.0e6$ and $1.0e5$ and two temperatures viz. $T = 300$ K and 200 K.

nucleated prior to transformation nucleated dislocations and their transfer into the continuum domain Ω_I^C at the interface. The pair of partials, as part of a full dislocation, can be identified from the atomic configurations by DXA [25], as discussed in Section 5. The radius of the atomistic region Ω_A should be more than the maximum stretch of the stacking fault. It has been experimentally observed in [54] that the stretch of the stacking fault for Ni can be anywhere between 15\AA and 50\AA .

To identify the optimal size of the atomistic region, concurrent simulations are conducted with a fixed overall domain of dimensions $200\text{ nm} \times 200\text{ nm} \times 4.22\text{ nm}$, containing a cylindrical atomistic region of radius $R_A = 50\text{ nm}$. This is shown in Fig. 10. From the first few dislocations shown in Fig. 10(a), it is observed that the stretch of the stacking fault reaches a maximum length at the onset of nucleation of the trailing partial. The stretch of the stacking fault reduces drastically once the trailing partial nucleates, and the full dislocation moves away from the crack tip.

The evaluation of the maximum stretch of stacking fault is considered for two different strain-rates, viz. $\dot{\epsilon} = 1.0e6$ and $1.0e5$, and for two temperatures $T = 300$ K and 200 K. Fig. 10(b) shows the distribution of the stacking fault width during nucleation of the first five dislocations for the different strain-rates and temperatures. The maximum stacking fault width is observed to be 27 nm for $\dot{\epsilon} = 1.0e6$ and $T = 200$ K. This width is in general, much larger than the equilibrium stacking fault width given in [54]. The large stretch of the stacking fault is attributed to the high stress-field gradient near the crack tip and also to the highly non-equilibrium process of dislocation nucleation. Based on these stacking fault width estimates, the size of the atomistic region for all subsequent simulations is chosen to be $R_A = 40\text{ nm}$.

7.3. Optimal width of the interface domain Ω_I

The width of the interface domain Ω_I plays an important role in the solution convergence-rate of the concurrent model. It is directly related to the number of atoms contained in each cluster pertaining to the node-atom connectivity at the interface, shown in Fig. 2. A small number of atoms in each cluster will introduce a large noise in the displacements of interface nodes due to atomic vibrations. Large fluctuations in these nodal displacements during iterations introduce large strains in elements that are closest to the interface and smallest in the continuum domain Ω_C . This in turn leads to poor solution convergence with imposed kinematic constraints at the interface. A large interface width, on the other hand, will increase the total number of degrees of freedom in the atomistic region Ω_A and raise the computational cost of the MD model. An optimal width of Ω_I is hence desirable, which is estimated from convergence trends of simulations with different interface widths.

The convergence-rate is estimated by solving the coupled model with a displacement-controlled loading on the outer boundary of the continuum region Ω_C . This corresponds to a biaxial strain field $\epsilon_{xx} = \epsilon_{yy} = 0.5\%$. The temperature of the atomic region is maintained at $T = 300$ K. A normalized displacement error of the interface nodes is defined as:

$$e_u^i = \frac{\|(\mathbf{u}_\beta^C)^i - (\mathbf{u}_\beta^A)^i\|}{\|(\mathbf{u}_\beta^C)^1 - (\mathbf{u}_\beta^A)^1\|} \quad (49)$$

where $\|\cdot\|$ corresponds to the L2 norm, $(\mathbf{u}_\beta^C)^i$ is the displacement solution of a FE node β and $(\mathbf{u}_\beta^A)^i$ is the average displacement of the associated cluster of atoms in Ω_I after i iterations. The normalizing factor in the denominator

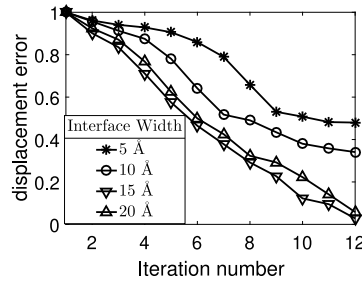


Fig. 11. Convergence in the displacement solution of interface nodes with iterations, for determining the optimal width of interface domain Ω_I . The results are for a domain with overall size $200 \text{ nm} \times 200 \text{ nm} \times 4.22 \text{ nm}$ with applied bi-axial strain $\epsilon_{xx} = \epsilon_{yy} = 0.005$ and temperature $T = 300 \text{ K}$.

Table 1

Values of parameters in the dislocation density crystal plasticity model in Section 3 for the continuum region Ω_C Keshavarz and Ghosh [21].

Parameter	Values	Parameter	Values	Parameter	Values
c_1	0.1	c_2	0.8	c_3	1.0×10^{-3}
c_4	1.0×10^{-4}	c_5	10.0	c_6	10.0
c_7	0.3	τ_c	110 MPa	ρ_c	1.0×10^{11}
b	2.49 \AA	Q	6.5×10^{-19}		

of Eq. (49) corresponds to the norm of the difference after the first iteration. A series of numerical simulations is performed by changing the interface width from 5 \AA to 20 \AA with an increment of 5 \AA . Fig. 11 shows the number of iterations needed to converge for different interface widths. For interface widths that are less than 10 \AA , the convergence rate is poor and the solution does not improve much after 10 iterations. This is due to the noise introduced in the computed average displacement of the cluster containing a small number of vibrating atoms. A steady improvement in the iterative solution is observed for interface widths greater than 15 \AA . Consequently, a width of 15 \AA is taken as optimal for all subsequent simulations. Since the optimal interface width depends on the temperature of the atomic region Ω_A due to atomic vibrations, it will be smaller at reduced temperatures.

A flow chart showing the sequence of steps in the coupled atomistic–continuum model is given in Fig. 12.

8. Validation of the concurrent model with a full MD model

The atomistic–continuum concurrent model, involving MD and crystal plasticity FE simulations, is validated by comparing with results of full atomistic MD simulations.

A single crystal Ni specimen with an embedded through-thickness crack is modeled for validation of the concurrent model with pure MD simulation results. The computational domain with lattice orientations and boundary conditions is shown in Fig. 13(a). It has dimensions of $100 \text{ nm} \times 200 \text{ nm} \times 4.22 \text{ nm}$. For full atomistic simulations by a MD model, this domain corresponds to ~ 7.5 million Ni atoms with an FCC lattice structure. The lattice constant for Ni is $a_o = 3.52 \text{ \AA}$. The embedded crack in the xz -plane has an initial length $2a_o = 20 \text{ nm}$. It resides in the atomistic sub-domain Ω_A of the concurrent model, which is a cylindrical region of radius $R_A = 30 \text{ nm}$. The interface region Ω_I is an annular region with inner radius of 25 nm and outer radius of 35 nm respectively. The crack is introduced at the center of the atomistic domain by removing two layers of atoms on both sides of the crack plane. The lattice orientation of the specimen with respect to the global Cartesian coordinate system is $x \rightarrow [11\bar{2}]$, $y \rightarrow [111]$ and $z \rightarrow [1\bar{1}0]$. This specific crystal orientation has been shown in [38] to nucleate straight dislocations parallel to the crack tip. The continuum domain Ω_C is discretized into a FE mesh containing approximately 4000 nodes and 15000 4-noded constant strain tetrahedral (CST) elements. To avert volumetric locking with crystal plasticity FE models, the CST elements are stabilized through the introduction of *F-bar patches*, developed in [55].

The coefficients of the elasticity tensor \mathbb{C}^e for pure Ni have been calibrated in [13,14] corresponding to the EAM potential of the atomistic model. The crystal plasticity parameters used in the computational study are given in Table 1.

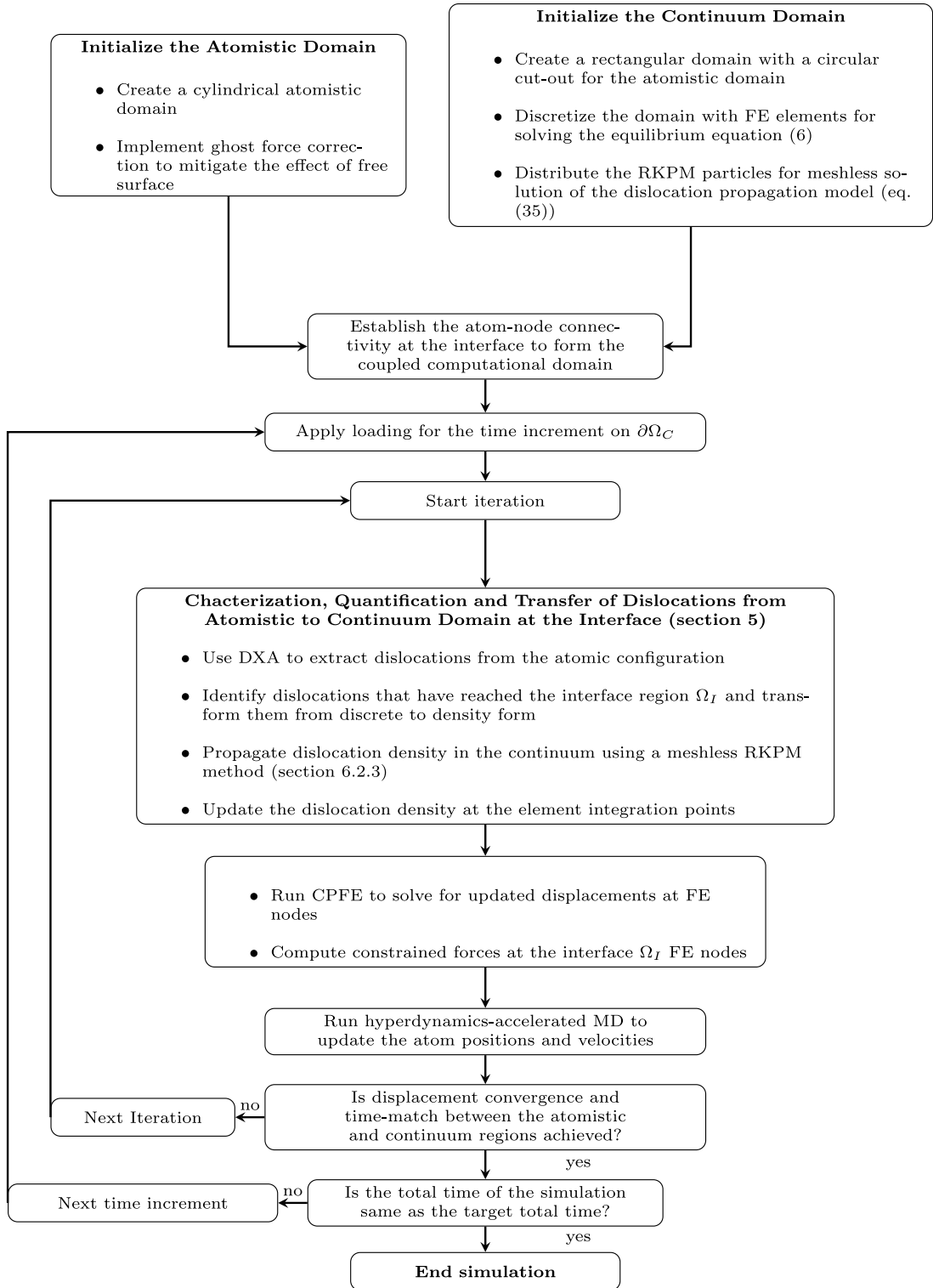


Fig. 12. Sequence of steps involved in the coupled, concurrent atomistic–continuum model.

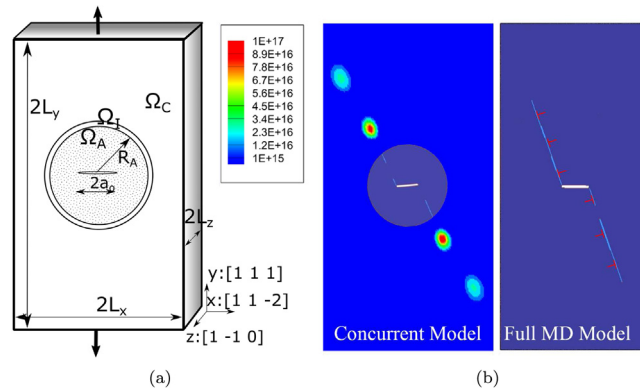


Fig. 13. Comparison of the performance of the concurrent model with the full MD model: (a) specimen details for the simulation, and (b) snapshot of dislocation configuration in the concurrent and MD models at an applied strain of $\epsilon_{yy} = 1.3\%$. The color of the continuum region represents the magnitude of the dislocation density (m^{-2}). The color of the atoms in the atomic region represents the common neighbor analysis (CNA) value of the corresponding atom [44]. Atoms with light blue color represent hcp stacking, while atoms with dark blue color represent FCC stacking. The local hcp stacking within an FCC crystal represents the stacking fault contained within the leading and trailing partial of a full dislocation. (For interpretation of the references to color in this figure legend, the reader is referred to the web version of this article.)

Both the concurrent and the full MD models are assumed to be free from any initial dislocation density. For the full MD model, simulations begin with static minimization of the whole system that is followed by the dynamic equilibration to achieve a stress-free state and temperature of 300 K. NPT ensemble is used for the dynamic equilibration. Next, displacement-controlled simulations are conducted by applying a uniaxial displacement controlled loading in the y direction at a constant strain-rate of $\dot{\epsilon} = 1.0e6 \text{ s}^{-1}$. A micro-canonical (NVE) ensemble is used for the MD simulations. The temperature of the atomic system is maintained at 300 K by using Langevin thermostat [41], and the z -direction pressure is kept to zero i.e. $\sigma_{zz} = 0.00$ by using a Berendsen barostat [56]. In this study, the NVE ensemble with a separate thermostat and barostat has been found to converge better than the NPT ensemble.

For the concurrent model, simulations begin with static minimization of the energy in the atomistic domain Ω_A , followed by dynamic equilibration. Subsequently the atom-node connectivity is established between nodes and atoms in the interface region Ω_I . Ghost force correction is introduced for the surface atoms in Ω_A^s to mitigate the free surface effect at the interface. Next, a uniaxial displacement controlled loading is applied on the boundary of the continuum domain Ω_C in the y direction at a constant strain-rate of $\dot{\epsilon} = 1.0e6 \text{ s}^{-1}$. The atomistic domain conditions are the same as for the full MD simulations.

8.1. Comparison of critical stress intensity factor for dislocation nucleation

The critical state for the onset of dislocation nucleation from the crack tip is measured by the mode-I stress intensity factor (SIF) K_I . The SIF for mode-I fracture is expressed as:

$$K_I = \sigma \sqrt{\pi a} \eta \quad (50)$$

where σ is the far-field stress on the external boundary of the continuum domain. The geometric factor η compensates for the finite size of the cracked specimen, and a polynomial given in [57] is used. The critical SIF value K_{IC} for nucleation of the first dislocation from the crack tip is found to be $0.705 \text{ MPa } \sqrt{\text{m}}$ and $0.71 \text{ MPa } \sqrt{\text{m}}$ respectively for the pure MD and concurrent models. This demonstrates a good agreement between the two models. The critical SIF for dislocation nucleation is also compared with an analytical solution given in [58,59]. This analytical model incorporates the influence of the large surface energy of the crack surface on the nucleation of dislocations. The corresponding SIF under mode-I loading is given as:

$$K_I = \sqrt{2\mu (\gamma_{us} + f\epsilon) \frac{Y}{1-\nu}} \quad (51)$$

Table 2

Material parameters associated with the analytical SIF model in Eq. (51) for Ni single crystal, obtained from [40,59].

Parameters	μ (GPa)	ν	γ_{us} (J m ⁻²)	f_0 (J m ⁻²)	$\delta f/\delta\epsilon$ (J m ⁻²)
Values	125	0.285	0.143	0.816	2.223

Table 3

Comparison of the critical SIF (in MPa $\sqrt{\text{m}}$) for nucleation of the first leading partial from a crack tip by the analytical, MD and concurrent models.

Models	Analytical	MD	Concurrent
K_{IC} (MPa $\sqrt{\text{m}}$)	0.661	0.705	0.71

where $f\epsilon$ is the surface correction term, in which f is considered to be a surface stress and ϵ is the crack tip strain. The higher-order effect due to the large crack tip strain is incorporated by expanding f about $\epsilon = 0$, i.e. $f \approx f_0 + \frac{1}{2}(\partial f/\partial\epsilon)\epsilon$. μ , ν and γ_{us} are respectively the shear modulus, Poisson's ratio and the unstable stacking fault energy of the material. Y is a geometric factor that accounts for the angle of inclination (θ) between the crack plane and the slip plane, which has been expressed as $Y = \frac{8}{(1+\cos\theta)\sin^2\theta}$ in [59]. Values of these material parameters for Ni, extracted from [40,59], are given in Table 2. Results of the critical SIF for dislocation nucleation by the analytical, full MD and concurrent models are compared in Table 3.

8.2. Comparison of nucleated dislocation density

The evolution of nucleated dislocation density by the concurrent model is compared with that by the MD model in this section. The performance of the concurrent model is assessed beyond the nucleation of the first dislocation. The dislocation density for the full MD model is computed as:

$$\rho_{MD} = l_{MD}/V \quad (52)$$

where l_{MD} is the total dislocation length within the entire computational domain and V is the volume of the computational domain. To obtain the total length l_{MD} of all the dislocations, the DXA [25] is used for extracting the dislocations from the atomic configuration. Once dislocations are identified in the form of dislocation beads and length-segments, the total length of the dislocations is computed as $l_{MD} = \sum_{i=1}^{N_l} \|d\mathbf{l}_i\|$, where $\|d\mathbf{l}_i\|$ is the length of the i th dislocation segment and N_l is the total number of dislocation segments present in the domain.

The dislocation density for the concurrent model is computed as:

$$\rho_{concurrent} = \frac{1}{V} \left[\sum_{i \in \Omega_A} \|d\mathbf{l}_i\| + \int_{\Omega_C} \rho_{nuc} d\Omega \right] \quad (53)$$

In Eq. (53) the first term corresponds to the total length of dislocation segments within the atomistic domain Ω_A including the interface Ω_I region. The second term computes the volume integral of the nucleated dislocation density within the continuum. The integral in the second term is evaluated over particles in the SPH domain as:

$$\int_{\Omega_C} \rho_{nuc} d\Omega = \sum_{p \in \Omega_C} \left[\sum_{q=1}^{N_p} \rho_{nuc}^q \bar{W}(\mathbf{x}_p - \mathbf{x}_q, h) \omega_q \right] \omega_p \quad (54)$$

The first summation is over all the SPH particles in the continuum domain Ω_C . In the second summation, N_p is the number of SPH particles within a support domain of the kernel function of the p th particle. $\bar{W}(\mathbf{x}_p - \mathbf{x}_q, h)$ is the RKPM kernel function of the p th particle evaluated at the location of the q th particle, and ω_p and ω_q are the weights associated with the particles p and q respectively. ρ_{nuc}^q is the SPH solution for nucleated dislocation density at q th particle.

Fig. 14 compares the evolution of the nucleated dislocation density by the concurrent and full MD models. The jumps in the dislocation density in the MD model correspond to the nucleation of new dislocations at the crack tip.

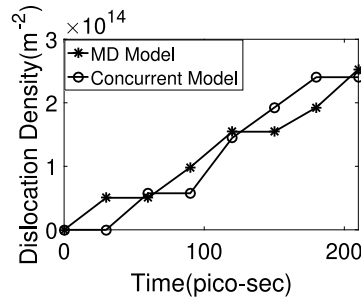


Fig. 14. Comparison of the evolution of the dislocation density between the concurrent model and the MD model.

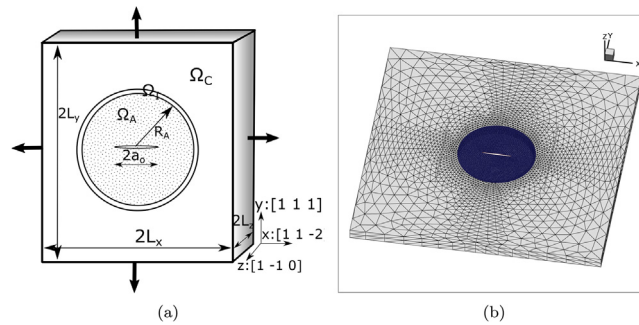


Fig. 15. Computational specimen modeled by the concurrent atomistic–continuum model for crack propagation: (a) specimen geometry with dimensions and loading, and (b) discretization of the atomistic and the continuum domain.

The orientation of the crystal with respect to the crack tip and the small z -thickness make the nucleated dislocations straight and extending through the thickness. While the dislocation densities predicted by the two models are in reasonably good agreement, a small difference is seen in the nucleation time of successive dislocations. Dislocation nucleation is a stress driven and thermally activated process. Hence, the nucleation time predicted by the coupled model with its assumptions is expected to be slightly different from that by pure MD, especially for finite temperature simulations.

9. Analytical evolution law for crack-tip nucleated dislocations

The concurrent atomistic-crystal plasticity model is used to derive an evolution law for the nucleated dislocation density due to a crack. As shown in Fig. 15(a), the single crystal Ni specimen model has dimensions of $200 \text{ nm} \times 200 \text{ nm} \times 4.22 \text{ nm}$ with a centrally embedded through-thickness crack of length $2a_0 = 20 \text{ nm}$. The figure shows the boundary conditions and the lattice orientation of the crystalline material. From discussions in Section 7.2, the atomistic domain Ω_A is configured as a cylindrical region with radius $R_A = 40 \text{ nm}$, and the interface region Ω_I is an annular region with inner and outer radii 35 nm and 45 nm respectively. The atomistic region contains about 2.5 million Ni atoms with FCC lattice structure. The lattice constant of Ni is $a_0 = 3.52 \text{ \AA}$. The lattice orientation of the specimen with respect to the global axis is $x \rightarrow [11\bar{2}]$, $y \rightarrow [111]$ and $z \rightarrow [1\bar{1}0]$.

For incorporating defects in the perfect Ni crystal, a small volume fraction of voids are randomly dispersed in the atomistic domain Ω_A by randomly removing 0.1% of the total atoms from the perfect crystal. The continuum domain Ω_C is discretized into a finite element mesh containing approximately 5000 nodes and 20000 stabilized 4-noded CST elements. A cylindrical region of radius 70 nm from the center of the crack is considered as free of initial dislocation density. The rest of the continuum region contains a constant distribution of initial dislocation density of 10^{15} m^{-2} . The strain-boost hyperdynamics potential is applied to a group of atoms in a through-thickness cylindrical region of radius 15 \AA near the crack-tip. The crystal plasticity parameters used for modeling the continuum domain are given in Table 1.

Fig. 16 shows snapshots of the dislocation structure in the concurrent model at two applied macroscopic strains, viz. $\epsilon_{11} = \epsilon_{22} = 3.1\%$ and $\epsilon_{11} = \epsilon_{22} = 3.4\%$. Dislocation nucleation and crack propagation do not start

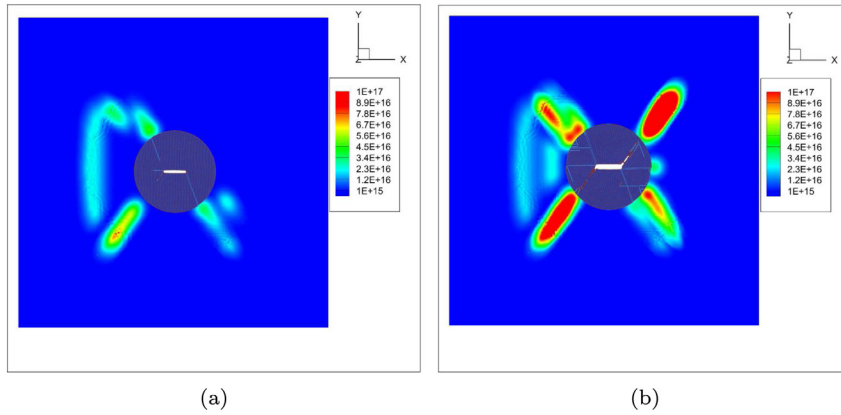


Fig. 16. Contour plots of the dislocation density (m^{-2}) in the concurrent model at macroscopic strains: (a) $\epsilon_{11} = \epsilon_{22} = 3.1\%$, and (b) $\epsilon_{11} = \epsilon_{22} = 3.4\%$.

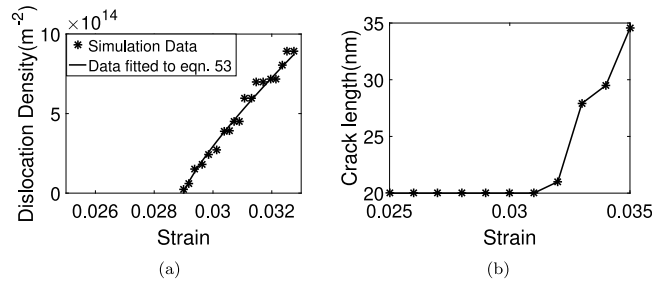


Fig. 17. Plots showing the evolution of: (a) dislocation density, and (b) crack length, as a function of the applied strain at a strain-rate $\dot{\epsilon} = 1.0e6$.

together at the same macroscopic strain. It is observed that the first dislocation nucleates at an applied strain of $\epsilon_{11} = \epsilon_{22} \approx 2.9\%$, while crack propagation commences at a strain of $\epsilon_{11} = \epsilon_{22} \approx 3.1\%$.

Fig. 17(a) plots the evolution of the dislocation density as a function of the macroscopic strain for an applied strain-rate of $\dot{\epsilon} = 1.0e6$. At the onset, several dislocations are seen to nucleate in quick succession. The macroscopic strain corresponding to nucleation of the first dislocation is $\epsilon_{11} = \epsilon_{22} \approx 2.9\%$. The critical SIF for dislocation nucleation at this macroscopic strain is evaluated by Eq. (50) to be $\approx 1.26 \text{ MPa } \sqrt{\text{m}}$. Fig. 17(b) plots the evolution of the crack length as a function of the applied macroscopic strain. The crack starts to propagate at a critical applied strain of $\epsilon_{11} = \epsilon_{22} \approx 3.1\%$. The simulation is terminated when the crack nearly reaches the boundary of the interface region Ω_I . Fig. 16(b) shows that the initial crack in the xz -plane bends away at an angle of 70.5° , which corresponds to a slip plane. It is observed that the crack does not evolve symmetrically from both the crack-tips.

The results of simulations with the concurrent model are used to generate a database of dislocation density as a function of the evolving strain. This data is used to develop an equation for dislocation density evolution, expressed as:

$$\rho_{nucl} = a_1 \rho_0 (\epsilon - \epsilon_c)^{a_2} \mathcal{H}(K - K_{IC}) \quad (55)$$

where K_{IC} is the critical SIF for nucleation of the first dislocation and a_1 and a_2 are material parameters. ρ_0 is the reference dislocation density, which has a value of 1.0^{14} m^{-2} and \mathcal{H} is the Heaviside step function.

Since the atomistic part of the concurrent model is enhanced by the strain-boost hyperdynamics time acceleration method, it is possible to study the nucleation process at much lower strain-rates than for conventional MD simulations. The lowest strain-rate studied here is $\dot{\epsilon} = 5.0e4$. Values of crack related parameters are investigated for three strain-rates, viz. $\dot{\epsilon} = 1.0e6$, $1.0e5$ and $5.0e4$. The calibrated values of crack related dislocation density parameters are reported in Table 4. ϵ_c is a critical strain corresponding to the critical SIF value. The numerical value of ϵ_c is obtained from the simulation by identifying the value of ϵ at the instance the SIF reaches the critical

Table 4

Calibrated values of the dislocation density parameters in Eq. (55), from simulations with the concurrent model at different strain-rates.

Strain rate $\dot{\epsilon}$ (s^{-1})	K_{IC} (MPa $\sqrt{\text{m}}$)	a_1	a_2
$1.0e6$	1.260	8.5	0.82
$1.0e5$	1.245	7.5	0.78
$5.0e4$	1.230	7.1	0.75

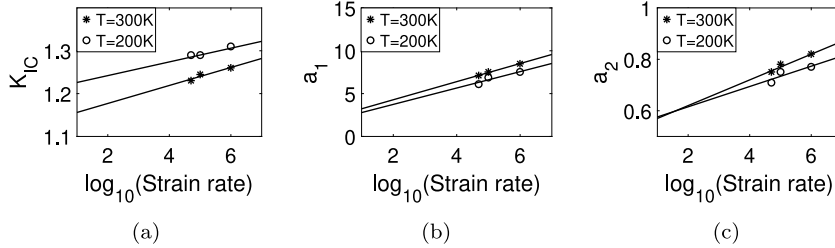


Fig. 18. Applied strain-rate (in logarithmic scale) and temperature dependence of: (a) critical stress intensity factor (K_{IC}), (b) parameter a_1 and (c) parameter a_2 in Eq. (55).

value K_{IC} . Table 4 shows that the values of K_{IC} are similar for the strain-rates, but the parameters a_1 and a_2 vary considerably with applied strain-rate. This implies that the state corresponding to nucleation of the first dislocation is almost the same and can be effectively represented by critical SIF values. The subsequent evolution of dislocation densities however, has strong dependence on the strain-rate.

Fig. 18 shows the strain-rate and temperature dependence of the parameters K_{IC} , a_1 and a_2 . It is seen that K_{IC} has a mild dependence on the strain-rate, but a strong dependence on the temperature. On the hand, the effect of strain-rate on a_1 and a_2 is more prominent in comparison with temperature.

10. Summary and conclusions

A coupled, concurrent atomistic–continuum multiscale model is developed in this paper to study the effects of a crack on dislocation evolution in crystalline metallic materials. The atomistic region of the concurrent model is simulated by the molecular dynamics (MD) code LAMMPS, whereas the continuum region is modeled by a dislocation density crystal plasticity FE model. The concurrent multiscale model incorporates a variety of modules, necessary for seamless coupling of the two distinct domains. A robust method is developed to characterize and quantify discrete dislocations from atomic configurations in the atomistic region, and subsequently transfer them to the continuum domain through transformation in the form of dislocation densities. A strain-boost hyperdynamics time acceleration method is implemented to conduct atomistic simulations at the lower strain-rates of continuum deformation. This time acceleration enables a time-scale match between the atomistic and continuum domains for compatible strain-rates in the concurrent model. The DXA method is used to identify and extract discrete dislocations in the atomic configurations. A novel method is developed for propagating dislocation densities in the continuum region by solving the advection equation for a scalar conserved quantity. The particle-based reproducing kernel particle method (RKPM), in conjunction with a collocation method and nodal integration, is implemented for solving the advection equation. To improve numerical efficiency, the propagation model is solved only in the localized regions of the dislocation core and its surroundings.

The concurrent atomistic–continuum model is validated with results of full MD simulations. Specifically, the evolution of dislocation densities and the critical stress intensity factor (SIF) are used to assess the performance of the concurrent model. The evolving dislocation densities in the concurrent model generally match those in the full MD model. The critical SIF for dislocation nucleation in the concurrent model is found to be within a 0.7% of the SIF predicted by the MD model. Results from the concurrent model are used to develop an analytical model for the crack-tip nucleated dislocation density evolution as a function of applied strain. This evolution law can be used to augment conventional dislocation density crystal plasticity models near the crack tip. Three parameters in

this model are studied for their temperature and strain-rate dependence. All of them show a stronger dependence on strain-rate in comparison with temperature.

While this paper introduces a comprehensive multiscale approach for coupling atomistic and continuum scales of crystal plasticity, additional tools can be developed for enhancing the accuracy, efficiency and versatility of the model. Extending the model to more realistic 3D crack configurations and longer propagation regimes will require additional concepts of adaptive mesh enhancement and adaptive evolution of the atomistic domain. Also, this generalized framework can be applied to investigate other crystalline materials and the effect of alloying elements. A primary goal of this concurrent atomistic-crystal plasticity model is to develop self-consistent, physics-based phase-field and crystal plasticity models for meso-scale modeling crack evolution in crystalline materials. This will be pursued in future studies.

Declaration of competing interest

The authors declare that they have no known competing financial interests or personal relationships that could have appeared to influence the work reported in this paper.

Acknowledgments

This work has been supported by the Office of Naval research, USA through Grant No. N00014-18-1-2596 (Program Director: Dr. William Mullins) and by the Air Force Office of Scientific Research Structural Mechanics and Prognosis Program, USA through Grant No. FA-RT1645 (Program Director: Dr. J. Tiley). Computing support from Maryland Advanced Research Computing Center (MARCC), USA is gratefully acknowledged.

Appendix. Computing the elasto-plastic tangent stiffness matrix

The elasto-plastic tangent stiffness matrix \mathbb{C}^t for the crystal plasticity material model is derived by a procedure given in [55,60] as:

$$\mathbb{C}^t = \frac{1}{\det \mathbf{F}_0^t} (\mathbf{F}_0^t \otimes \mathbf{F}_0^t) : \mathbb{C}^0 : (\mathbf{F}_0^t \otimes \mathbf{F}_0^t) \quad (\text{A.1})$$

where

$$\mathbb{C}^0 = \frac{\partial \mathbf{S}_0^t}{\partial \mathbf{E}_0^t} = (\det \mathbf{F}^p) (\mathbf{F}^p \otimes \mathbf{F}^p)^{-1} : \left\{ \frac{\partial \mathbf{S}^*}{\partial \mathbf{E}} + \left[\mathbf{S}^* \otimes \mathbf{F}^{p-T} - (\det \mathbf{F}^{p-1}) \left[\mathbf{I} \otimes (\hat{\mathbf{S}} \mathbf{F}^{pT})^T + (\mathbf{F}^p \hat{\mathbf{S}}) \otimes \mathbf{I} \right] \right] : \frac{\partial \mathbf{F}^p}{\partial \mathbf{E}} \right\} \quad (\text{A.2a})$$

$$\mathbf{S}^* = (\det \mathbf{F}^p)^{-1} \mathbf{F}^p \hat{\mathbf{S}} \mathbf{F}^{pT} \quad (\text{A.2b})$$

$$\frac{\partial \mathbf{S}^*}{\partial \mathbf{E}} = \left[\mathbf{I} \otimes \mathbf{I} + \sum_{\alpha}^{N_{slip}} \left\{ \mathbb{C}^{\alpha} \otimes \frac{\partial \Delta \gamma^{\alpha}}{\partial \mathbf{S}^*} \right\} \right]^{-1} \left[\mathbf{A}^{\alpha} - \sum_{\alpha}^{N_{slip}} \Delta \gamma^{\alpha} \mathbf{B}^{\alpha} \right] \quad (\text{A.2c})$$

$$\mathbf{A}^{\alpha} = \mathbb{C}^e : (\mathbf{F}^{p-1} \otimes \mathbf{F}^{p-1}) \quad (\text{A.2d})$$

$$\mathbf{B}^{\alpha} = \mathbb{C}^e : \left[\mathbf{F}^{p-T} \otimes (\mathbf{F}^{p-T} s_0^{\alpha})^T + (\mathbf{F}^{p-T} s_0^{\alpha})^T \otimes \mathbf{F}^{p-T} \right] \quad (\text{A.2e})$$

$$\frac{\partial \mathbf{F}^p}{\partial \mathbf{E}} = \sum_{\alpha}^{N_{slip}} (s_0^{\alpha} \mathbf{F}^p) \otimes \left(\frac{\partial \Delta \gamma^{\alpha}}{\partial \mathbf{S}} \frac{\partial \mathbf{S}^*}{\partial \mathbf{E}} \right) \quad (\text{A.2f})$$

where \mathbb{C}^e is the fourth-order anisotropic elasticity tensor. The symbols $\underline{\otimes}$ and $\overline{\otimes}$ represent lower and upper tensor products, defined as $(A \underline{\otimes} B)_{ijkl} = A_{ik} B_{jl}$ and $(A \overline{\otimes} B) = A_{il} B_{jk}$ respectively. The increment of the slip $\Delta \gamma^{\alpha}$ on each slip system is computed from its rate given in Eq. (18) as $\Delta \gamma^{\alpha} = \dot{\gamma}^{\alpha} \Delta t$, where Δt is the time increment.

References

- [1] A. Needleman, An analysis of tensile decohesion along an interface, *J. Mech. Phys. Solids* 38 (1990) 289–324.
- [2] M. Ortiz, A. Pandolfi, Finite-deformation irreversible cohesive element for three-dimensional crack-propagation analysis, *Internat. J. Numer. Methods Engrg.* 44 (1999) 1267–1282.
- [3] K.L. Roe, T. Siegmund, An irreversible cohesive zone model for interface fatigue crack simulation, *Eng. Fract. Mech.* 70 (2003) 209–232.
- [4] T. Zhu, J. Li, S. Yip, Atomistic study of dislocation loop emission from a crack tip, *Phys. Rev. Lett.* 93 (2) (2004) 025503–1–025503–4.
- [5] Y. Shimomura, M. Kiritani, I. Mukouda, Computer simulation study of the atomistic mechanism of deformation and fracture initiation in thin fcc metal films, *Mater. Sci. Eng. A* 350 (1–2) (2003) 238–244.
- [6] J. Zhang, S. Ghosh, Molecular dynamics based study and characterization of deformation mechanisms near a crack, *J. Mech. Phys. Solids* 61 (2013) 1670–1690.
- [7] X.W. Zhou, J.A. Zimmerman, E.D. Reedy Jr., N.R. Moody, Molecular dynamics simulation based cohesive surface representation of mixed mode fracture, *Mech. Mater.* 40 (2008) 832–845.
- [8] R.E. Miller, E.B. Tadmor, A unified framework and performance benchmark of fourteen multiscale atomistic/continuum coupling methods, *Modelling Simul. Mater. Sci. Eng.* 17 (2009) 053001.
- [9] E.B. Tadmor, *The Quasicontinuum Method* (PhD thesis), Brown University, 1996.
- [10] V.B. Shenoy, R. Miller, E.B. Tadmor, D. Rodney, R. Phillips, M. Ortiz, An adaptive finite element approach to atomic-scale mechanics-the quasicontinuum method, *J. Mech. Phys. Solids* 47 (3) (1999) 611–642.
- [11] S. Badia, P. Bochev, R. Lehoucq, J. Parks, M. Fish, M.A. Nuggehally, M. Gunzburger, A force-based blending model for atomistic-to-continuum coupling, *Int. J. Multiscale Comput. Eng.* 5 (5) (2007) 387–406.
- [12] E. Saether, V. Yamakov, E.H. Glaessgen, An embedded statistical method for coupling molecular dynamics and finite element analyses, *Internat. J. Numer. Methods Engrg.* 78 (11) (2009) 1292–1319.
- [13] S. Ghosh, J. Zhang, Elastic crack propagation model for crystalline solids using a self-consistent coupled atomistic-continuum framework, *Int. J. Fract.* 208 (2017) 171–189.
- [14] J. Zhang, S. Chakraborty, S. Ghosh, Concurrent atomistic-continuum model for developing self-consistent elastic constitutive modeling of crystalline solids with crack, *Int. J. Multiscale Comput. Eng.* 15 (2017) 99–119.
- [15] S. Chakraborty, S. Ghosh, Hyperdynamics accelerated concurrent atomistic-continuum model for developing crack propagation models in elastic crystalline materials, *Comput. Mater. Sci.* 154 (2018) 212–224.
- [16] L. Xiong, Q. Deng, G. Tucker, D.L. McDowell, Y. Chen, A concurrent scheme for passing dislocations from atomistic to continuum domains, *Acta Mater.* 60 (3) (2012) 899–913.
- [17] I. Tembhekar, J.S. Amelang, L. Munk, D.M. Kochmann, Automatic adaptivity in the fully nonlocal quasicontinuum method for coarse-grained atomistic simulations, *Internat. J. Numer. Methods Engrg.* 110 (9) (2017) 878–900.
- [18] G. Anciaux, T. Junge, M. Hodapp, J. Cho, J.-F. Molinari, W.A. Curtin, The Coupled Atomistic/Discrete-Dislocation method in 3d part I: Concept and algorithms, *J. Mech. Phys. Solids* 118 (2018) 152–171.
- [19] B. Eidel, A. Stukowski, A variational formulation of the quasicontinuum method based on energy sampling in clusters, *J. Mech. Phys. Solids* 57 (1) (2009) 87–108.
- [20] A. Ma, F. Roters, A constitutive model for fcc single crystals based on dislocation densities and its application to uniaxial compression of aluminium single crystals, *Acta Mater.* 52 (12) (2004) 3603–3612.
- [21] S. Keshavarz, S. Ghosh, Hierarchical crystal plasticity fe model for nickel-based superalloys: Sub-grain microstructures to polycrystalline aggregates, *Int. J. Solids Struct.* 55 (2015) 17–31.
- [22] A. Ma, F. Roters, D. Raabe, A dislocation density based constitutive model for crystal plasticity fem including geometrically necessary dislocations, *Acta Mater.* 54 (8) (2006) 2169–2179.
- [23] S. Keshavarz, S. Ghosh, A.C.E. Reid, S.A. Langer, A non-schmid crystal plasticity finite element approach to multi-scale modeling of nickel-based superalloys, *Acta Mater.* 114 (2016) 106–115.
- [24] S. Keshavarz, S. Ghosh, Multi-scale crystal plasticity finite element model approach to modeling nickel-based superalloys, *Acta Mater.* 61 (17) (2013) 6549–6561.
- [25] A. Stukowski, K. Albe, Extracting dislocations and non-dislocation crystal defects from atomistic simulation data, *Modelling Simul. Mater. Sci. Eng.* 18 (2010) 085001.
- [26] W.K. Liu, S. Jun, Y.F. Zhang, Reproducing kernel particle methods, *Internat. J. Numer. Methods Fluids* 20 (8–9) (1995) 1081–1106.
- [27] W.K. Liu, Y. Chen, S. Jun, J.S. Chen, T. Belytschko, R.A. Pan, C. Uras, C.T. Chang, Overview and applications of the reproducing kernel particle methods, *Arch. Comput. Methods Eng.* 3 (1996) 3–80.
- [28] S.J. Plimpton, Fast parallel algorithms for short-range molecular dynamics, *J. Comput. Phys.* 117 (1995) 1–19.
- [29] S. Ghosh, *Micromechanical Analysis and Multi-Scale Modeling Using the Voronoi Cell Finite Element Method*, CRC Press/Taylor & Francis, 2011.
- [30] K.J. Bathe, *Finite Element Procedures*, Prentice Hall, Pearson Education Inc., 2006.
- [31] U.F. Kocks, A.S. Argon, A.F. Ashby, *Thermodynamics and kinetics of slip*, Oxford, 1975.
- [32] D. Hull, D.J. Bacon, *Introduction to Dislocations*, Elsevier, 2011.
- [33] D.W. Lee, H. Kim, A. Strachan, M. Koslowski, Effect of core energy on mobility in a continuum dislocation model, *Phys. Rev. B* 83 (104101) (2011).
- [34] J.F. Nye, Some geometrical relations in dislocated crystals, *Acta Metall.* 1 (2) (1953) 153–162.
- [35] D.J. Luscher, J.R. Mayeur, H.M. Mourad, A. Hunter, M.A. Kenamond, Coupling continuum dislocation transport with crystal plasticity for application to shock loading conditions, *Int. J. Plast.* 76 (2016) 111–129.

- [36] J.R. Mayeur, H.M. Mourad, D.J. Luscher, A. Hunter, M.A. Kenamond, Numerical implementation of a crystal plasticity model with dislocation transport for high strain rate applications, *Modelling Simulation Mater. Sci. Eng.* 24 (4) (2016) 045013.
- [37] S. Hara, J. Li, Adaptive strain-boost hyperdynamics simulations of stress-driven atomic processes, *Phys. Rev. B* 82 (184114) (2010).
- [38] S. Chakraborty, J. Zhang, S. Ghosh, Accelerated molecular dynamics simulations for characterizing plastic deformation in crystalline materials with crack, *Comput. Mater. Sci.* 121 (2016) 23–34.
- [39] S. Chakraborty, Development of a Self-Consistent Coupled Atomistic-Continuum Model to Study the Brittle and Ductile Fracture in Metallic Materials (PhD thesis), Johns Hopkins University, 2020.
- [40] Y. Mishin, D. Farkas, M.J. Mehl, D.A. Papaconstantopoulos, Interatomic potentials for monoatomic metals from experimental data and *ab initio* calculations, *Phys. Rev. B* 59 (3393) (1999).
- [41] B. Dunweg, W. Paul, Brownian dynamics simulations without Gaussian random numbers, *Internat. J. Modern Phys. C* 02 (03) (1991) 817–827.
- [42] A.F. Voter, Hyperdynamics: Accelerated molecular dynamics of infrequent events, *Phys. Rev. Lett.* 78 (3908) (1997).
- [43] V. Yamakov, D.H. Warner, E. Zamora, W.A. Curtin, E.H. Glaessgen, Investigation of crack tip dislocation emission in aluminum using multiscale molecular dynamics simulation and continuum modeling, *J. Mech. Phys. Solids* 65 (2014) 35–53.
- [44] D.J. Honeycutt, H.C. Anderson, Molecular dynamics study of melting and freezing of small Lennard-Jones clusters, *J. Chem. Phys.* 91 (1987) 4950–4963.
- [45] J.P. Hirth, J. Lothe, *Theory of Dislocations*, Krieger, 1982.
- [46] R.A. Gingold, J.J. Monaghan, Smoothed particle hydrodynamics: theory and application to non-spherical stars, *Mon. Not. R. Astron. Soc.* 181 (3) (1977) 375–389.
- [47] N.R. Aluru, A point collocation method based on reproducing kernel approximations, *Internat. J. Numer. Methods Engrg.* 47 (6) (2000) 1083–1121.
- [48] S. Beissel, T. Belytschko, Nodal integration of element free Galerkin method, *Comput. Methods Appl. Mech. Engrg.* 139 (1996) 49–74.
- [49] D.S. Balsara, Von Neumann stability analysis of smoothed particle hydrodynamics—suggestions for optimal algorithms, *J. Comput. Phys.* 121 (2) (1995) 357–372.
- [50] S. Dai, J.C.M. Li, Dislocation-free zone at the crack tip, *Scr. Metall.* 16 (2) (1982) 183–188.
- [51] M. Tanaka, S. Sadamatsu, G.S. Liu, H. Nakamura, K. Higashida, I.M. Robertson, Sequential multiplication of dislocation sources along a crack front revealed by high-voltage electron microscopy and tomography, *J. Mater. Res.* 26 (4) (2011) 508–513.
- [52] M. Huang, L. Zhao, J. Tong, Discrete dislocation dynamics modelling of mechanical deformation of nickel-based single crystal superalloys, *Int. J. Plast.* 28 (1) (2012) 141–158.
- [53] C.T. Sun, Z.H. Jin, *Fracture Mechanics*, Elsevier, 2012.
- [54] C.B. Carter, S.M. Holmes, The stacking-fault energy of nickel, *Phil. Mag.* 35 (5) (1977) 1161–1172.
- [55] J. Cheng, A. Shahba, S. Ghosh, Stabilized tetrahedral elements for crystal plasticity finite element analysis overcoming volumetric locking, *Comput. Mech.* 57 (2016) 733–753.
- [56] H.J.C. Berendsen, J.P.M. Postma, W.F. van Gunsteren, A. DiNola, J.R. Haak, Molecular dynamics with coupling to an external bath, *J. Chem. Phys.* 81 (8) (1984) 3684–3690.
- [57] T.L. Anderson, *Fracture Mechanics: Fundamentals and Applications*, CRC press, 2005.
- [58] J.R. Rice, Dislocation nucleation from a crack tip: An analysis based on the Peierls concept, *J. Mech. Phys. Solids* 40 (2) (1992) 239–271.
- [59] J. Knap, K. Sieradzki, Crack tip dislocation nucleation in FCC solids, *Phys. Rev. Lett.* 82 (8) (1999).
- [60] F.T. Meissonnier, E.P. Busso, N.P. O'Dowd, Finite element implementation of a generalised non-local rate-dependent crystallographic formulation for finite strains, *Int. J. Plast.* 17 (4) (2001) 601–640.